Advances in Astronomy

Mars Climate Evolution, Habitability, Astrobiology, and Resources

Lead Guest Editor: Javier Martín-Torres
Guest Editors: Eriita Jones, Conor A. Nixon, Josep M. Trigo-Rodríguez, and Sanjay Vijendran

Mars Climate Evolution, Habitability, Astrobiology, and Resources

Advances in Astronomy

Mars Climate Evolution, Habitability, Astrobiology, and Resources

Lead Guest Editor: Javier Martín-Torres
Guest Editors: Eriita Jones, Conor A. Nixon, Josep M. Trigo-Rodríguez, and Sanjay Vijendran

Contents

Hindawi
Advances in Astronomy
Volume 2022, Article ID 6672456, 10 pages
https://doi.org/10.1155/2022/6672456

Research Article

Testing Correspondence between Areas with Hydrated Minerals, as Observed by CRISM/MRO, and Spots of Enhanced Subsurface Water Content, as Found by DAN along the Traverse of Curiosity

M. V. Djachkova, I. G. Mitrofanov, S. Y. Nikiforov, D. I. Lisov, M. L. Litvak, and A. B. Sanin

Space Research Institute of the Russian Academy of Sciences, Moscow, Russia

Correspondence should be addressed to M. V. Djachkova; djachkova@np.cosmos.ru

Received 4 December 2020; Revised 16 February 2022; Accepted 19 March 2022; Published 1 April 2022

Academic Editor: Josep M. Trigo-Rodríguez

Possible correlation is studied between Water Equivalent Hydrogen (WEH) in the Martian subsurface, as measured by the DAN (Dynamic Albedo of Neutrons) instrument along the Curiosity traverse, and the presence of hydrated minerals on the surface, as seen from the orbit by CRISM (Compact Reconnaissance Imaging Spectrometer for Mars) instrument onboard MRO (Mars Reconnaissance Orbiter). Cross-analysis of the subsurface WEH values from DAN passive measurements with the distribution of hydrated minerals over the surface of Gale crater according to Specialized Browse Product Mosaics is performed for the initial 20 km part of traverse. As a result, we found an increase up to 0.4 wt% of the mean WEH value for the surface areas with the spectral signatures of polyhydrated sulfates. The increase is shown to be higher with the more prominent spectral signature on the surface. Similar WEH increase for the two other types of hydrated minerals, such as monohydrated sulfates and phyllosilicates, was not found for the tested part of the traverse. Polyhydrated sulfates being a part of the sedimentary deposits composing the surface of Gale crater should have considerable thickness that is necessary for the subsurface neutron sensing by DAN measurements.

1. Introduction

Gale crater was presumably formed during the late Noachian period (about 3.7-3.8 Ga) as a result of a large meteorite impact [1]. Its radius is about 150 km, and its initial depth is thought to be about 5 km. In its evolutional history from formation to the modern time, one may conditionally distinguish two main stages [2, 3]. The first stage corresponds to the Noachian period with a possibly warm and humid climate on the planet (or at least with episodic warm conditions), when Mars had a rather dense atmosphere. During this stage, the crater could be occasionally filled up with water and turned into a lake, at the bottom of which weathering of primary rocks in contact with an alkaline water environment produced phyllosilicates [4, 5]. The first stage ended by the beginning of Late Hesperian, when the climate of Mars became close to modern, with a thin atmosphere and a dry and cold surface. By the end of the first stage, Gale crater is thought to be filled up with layered sedimentary deposits [6].

In the second stage, the sedimentary deposits filling Gale crater were exposed, probably by wind erosion, creating Mount Sharp—5.5 km tall central mound which is not related to the central peak formed during the impact event [7]. The lowest visible units of Mount Sharp contain a variety of minerals that are indicative of aqueous conditions. Phyllosilicate (including the groups smectite, vermiculite, illite, kaolinite, serpentine, micas, and chlorite, commonly called clay minerals) spectral signatures are observed in some stratigraphic units near the base of

Mount Sharp, and sulfate-bearing minerals (such as anhydrite, bassanite, gypsum, and jarosite) are observed in younger, stratigraphically higher sedimentary units [8, 9]. This mineralogical transition suggests that the conditions under which the sediments were deposited changed through time. The broad mineral stratigraphy with sulfate-bearing units overlying phyllosilicate-bearing units has been recognized in similarly aged deposits globally on Mars [10]. This mineralogical succession may mark the beginning of the transition from Noachian to Hesperian, e.g., from a relatively wet and warm early Mars to a very dry and cold modern Mars [8, 11].

Thus, the sediments on the modern surface of Gale crater represent a natural record of Mars hydrological evolution, where a study of the composition and sequence of sedimentary strata from the crater floor up to the top of its central mound allows the disclosing of the changes of environmental conditions along the chronology of their formation [6]. At present, the ground water in the Martian soil may precipitate from the current thin atmosphere forming multilayers of molecules on the grains of regolith (as adsorbed water) and filling the porosity volume between grains (as free water ice). Though there is no direct evidence of ground ice, indirect evidence for the formation of frost at the surface of Gale crater exists [12]. Therefore, both kinds of water might exist currently in the shallow subsurface of Gale crater: water in the form of chemically bound molecules in hydrated minerals and water as adsorbed molecules in the regolith.

The presence of water in the subsurface of Gale crater is proved by the DAN active neutron sensing experiment onboard the Curiosity rover [13–15]. This paper presents the results of the comparative analysis of subsurface water abundance, as derived from DAN passive measurements data [16], together with data for the surface minerals distribution, as measured by CRISM onboard MRO. This analysis is thought to allow distinguishing which kind of ground water most likely exists in the subsurface along the Curiosity traverse over the bottom of Gale crater.

2. DAN Measurements along the Rover Traverse

The DAN instrument is an active neutron detector for sensing the subsurface layer of about 60 cm thickness by pulses of 14 MeV neutrons, produced by the pulsing neutron generator—PNG [15]. Pulses of neutrons produce the postpulse emission or *Dynamic Albedo of Neutrons*. Two DAN neutron counters record the time profiles of postpulse total neutron emission: CTN at thermal and epithermal energy range and CETN at epithermal energy range.

Since hydrogen in the Martian subsurface is most likely a part of either hydroxyl or water molecules, its content is conventionally measured in terms of Water Equivalent Hydrogen (WEH). On the other hand, the content of the neutron absorbing nuclei in the subsurface is evaluated by a single measurable parameter of the so-called Absorption Equivalent Chlorine—AEC [17]. Chlorine is selected because it is considered the major contributor to neutron absorption in the Martian regolith. The value of AEC takes into account not only the mass fraction of chlorine itself, but also all other absorbers in the subsurface matter, if their mass fractions differ from the values predicted by the so-called "standard composition" model of the Martian soil [18].

DAN started operating on Mars on August 12, 2012, just after the rover landing [19]. The data for the current analysis were obtained since that time until November 2018. That corresponds to 2218 sols and 19 971 m distance along the traverse. According to the rover flight rules, DAN active operations are only allowed at rover stops. Thus, estimates of WEH and AEC based on active measurements are available for the rover parking spots only [13]. For the first 20 km part of the rover traverse until sol 2218, the mean WEH and AEC values are found to be (2.6 ± 0.7) wt% and (1.0 ± 0.1) wt%, respectively [13].

While PNG operates only during active sessions lasting for 15–30 minutes at stops, DAN counters are working almost continuously, both at rover stops and during drives. When PNG is off, neutron counters continuously measure the local neutron emission. Flux and energy spectra of the surface albedo neutrons produced both by the Multi-Mission Radioisotope Thermoelectric Generator and Galactic Cosmic Rays largely depend on the presence of hydrogen, measured as WEH, and neutron absorbers, measured as AEC, in the subsurface matter. Thus, DAN continuous passive measurements give an opportunity to determine the WEH value at any particular spot below the rover along the traverse [16].

A special procedure of DAN passive data processing has been developed based on the empirically found relationships between active and passive data, measured simultaneously at the total number of 328 rover stops (see [16], for details). This empirical relationship, as well as the knowledge on the AEC, is used for obtaining the continuous profile of WEH values. The physical size of an individual spot on the surface for passive neutron sensing is shown to be about 3 meters in diameter [17], so the physical resolution of WEH variations along the traverse could be associated with such scale.

Distances between the rover stops vary from several meters up to hundreds of meters. To estimate AEC between two stops along the traverse, one needs to make an additional assumption for the scale of AEC spatial variations. It was suggested by [16], to use two approaches. The first one assumes a long-range (LR) scaling of AEC variability, when a smooth interpolation of AEC value is thought to be applicable along the path from one stop to another. In this case, the AEC value at each point between two stops could be derived from the interpolated values of active measurements at these stops. The second approach postulates that AEC might vary at a scale of several meters or so, presuming a short-range (SR) scaling of the AEC variability. In this case, the AEC value at each intermediate point of the traverse between two stops is thought to be randomly distributed according to the entire data set of the active measurements. For the part of the rover traverse studied in this paper, the mean AEC value for all active measurements is found to be equal to (1.0 ± 0.1) wt%.

After processing DAN passive data until sol 2218, two continuous profiles of the WEH spatial variability were obtained with a distance resolution of 3 meters using LR and/or SR approaches (Figure 1). The WEH value was found

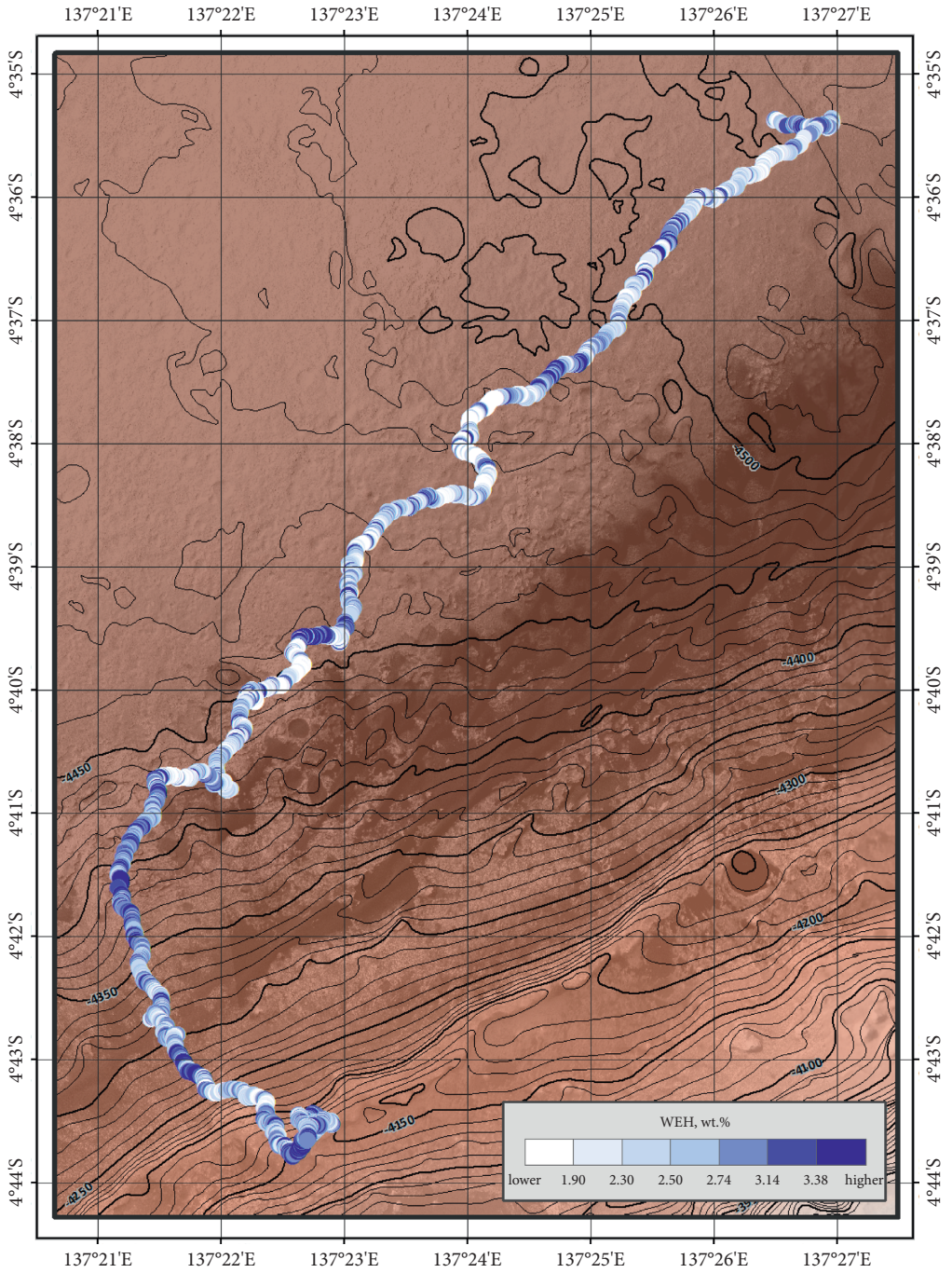

Figure 1: WEH as derived from DAN passive measurements using the LR approach for AEC variations along the Curiosity traverse.

to vary from around zero to 6.3 wt% [16]. These data were used for cross-analysis with CRISM spectral data products; see below.

3. CRISM Data Products for Cross-Analysis with DAN Data

CRISM instrument onboard the NASA MRO spacecraft performs imaging spectrometry in the visible and near-infrared wavelength range of 362–3920 nanometers. Such chemicals as iron, oxides, carbonates, etc. on the Martian surface have characteristic spectral features in the visible and infrared ranges and are distinguishable by CRISM [20].

For the current cross-analysis with DAN data, we used the publically available Specialized Browse Product Mosaics [21]. The CRISM team specifically created this data product for studying the Curiosity landing site. Hyperspectral images with high spatial resolution of about 20 m, not degraded by the increased noise or by atmosphere opacity, were selected as the source images for creating the products. Mathematical processing was applied to reflectance values at key wavelengths associated with diagnostic or indicative mineral

structure on the surface. The resulting composites of individual parameters reflect the thematic mineralogical diversity of the surface. A high value in the image plane indicates a relatively strong spectral feature for the particular product as compared to the range present regionally around the landing site [21].

In our study, two Specialized Browse Product Mosaic products were of special interest: "HYD" and "ALT." Both were constructed from images in the IR spectral range, as they characterize the spectral features of minerals that are thought to be formed by the interaction of rocks with liquid water. These two data products represent the surface distribution of such minerals as phyllosilicates (generally Fe-smectites) and mono- or polyhydrated Mg-sulfates (mostly kieserite and hexahydrite, respectively). The "HYD" data product shows indicators of hydrated minerals with a focus on the hydrated sulfates, while the "ALT" data product focuses on Fe/Mg phyllosilicates on the surface.

It should be taken into account that hydrated minerals, which are believed to be present in the shallow subsurface, might not be revealed by detection of their spectral indicators on the surface as they might be covered by dust or by a thin upper layer of some different mineralogical composition. While DAN senses the subsurface down to 1 m depth, CRISM images the uppermost layer of the Martian surface. However, the deposits of hydrated minerals that spread from the top down to the subsurface should be detectable by both instruments, CRISM from the orbit and DAN from the surface. To test the presence of such deposits and to map them along the rover, traverse was the goal of the performed cross-analysis, as presented below.

4. Cross-Analysis of DAN Passive Data with CRISM Data Products

The total number of 1028 CRISM mapping pixels, located along the traverse of the rover, was selected. For each such pixel with the size of about 20 meters, the mean WEH value was evaluated inside it according to the DAN passive measurements data, processed by the LR and SR approaches (see Section 3, Tables 1 and 2). Uncertainties of the WEH mean values were derived from the uncertainties of WEH values of the contributed distance intervals.

For each of the three types of hydrated minerals, such as phyllosilicates, monohydrated sulfates, and polyhydrated sulfates, the testing groups of corresponding CRISM pixels were selected, which manifest the spectral signatures of these minerals. Three groups with 51, 45, and 101 CRISM pixels were identified for phyllosilicates, monohydrated sulfates, and polyhydrated sulfate, respectively. The reference group of 831 CRISM pixels with no spectral signatures of any of the three types of hydrated minerals was also composed.

The method of cross-analysis of DAN and CRISM data is based on the comparison of the distribution of the mean WEH values for the testing group of CRISM pixels attributed to the particular testing mineral with the distribution of the mean WEH values for the reference group of CRISM pixels. As the simplest test, the average values and sample variances of WEH for the testing and the reference groups are compared. In addition, Pearson's chi-squared test is used for more precise testing of the statistical difference between them. Two distributions are thought to be statistically distinct, if the probability for their coincidence (p-level) is sufficiently small, $p < 0.001$.

One finds that there is no distinction of the distributions of WEH for groups of the CRISM pixels associated with either phyllosilicates or monohydrated sulfates from the reference group (Tables 1 and 2). For both cases of WEH estimation, using either LR or SR approach, the p-level values point out a rather good agreement between WEH distributions for testing and reference groups.

On the other hand, the evident effect of distinction from the reference group is found for the testing group of 101 CRISM pixels with the spectral signature of polyhydrated sulfates (Figure 2(a)). The differences between mean values of WEH are (0.2 ± 0.1) wt% for the LR approach (Table 1) and (0.4 ± 0.1) wt% for the SR approach (Table 2). According to Pearson's chi-squared test, the p-levels for the statistical coincidence between WEH distributions for the testing and reference groups are found to be much less than 0.001 (see Tables 1 and 2). Thus, the mean WEH value for the testing group of CRISM pixels, associated with the presence of polyhydrated sulfates, is confidently larger than the mean WEH value for the reference group of pixels, which do not have the spectral signature of such type of mineral.

It is reasonable to expect that the stronger spectral signature of the presence of minerals on the surface (seen as larger values in the RGB image plane) might correspond to a higher content of WEH detected by DAN in the subsurface. To check this assumption, the testing group of 101 CRISM pixels linked with polyhydrated sulfates was divided into two subgroups. The subgroup of "high intensity" includes pixels with the brightness >20 in the RGB image plane. Correspondingly, the subgroup of "low intensity" includes pixels with the brightness <20. The value of 20 was chosen as a dividing value for the total group into two statistically equal subgroups. For these two subgroups, the distributions of WEH were built, and their comparison with the reference distribution was performed (Tables 1 and 2).

Figure 3 shows the WEH distributions for the testing subgroups of CRISM pixels with "high intensity" polyhydrated sulfates for the cases of LR (a) and SR (b) approaches. The more pronounced shift to larger values is evident for the WEH distributions of "high intensity" subgroup in comparison with the WEH distribution for the reference group (Figure 3). Their mean WEH values become equal to (2.9 ± 0.1) wt% and (3.1 ± 0.1) wt% for the cases of LR and SR approaches, respectively. Besides, the Pearson test proves that WEH distributions for the "high intensity" subgroup of CRISM pixels are confidently distinct from the one for the reference group. The values of the p-level are much less than 0.001 (Tables 1 and 2).

As we stated in Section 2 of this paper, the value of WEH is not measured directly, but is obtained through the modelling of active and passive measurement data and is, therefore, model-dependent. To exclude the probable effects of model dependency, we performed the similar analysis as described above for the initial measured parameter of

Table 1: Comparison of parameters of WEH distributions for groups of CRISM pixels. WEH is derived from the DAN passive data for the case of long-range variability of AEC (LR case).

Groups of CRISM pixels		Coverage of the traverse (%)	Number of CRISM pixels	Number of DAN measurements	Mean of the WEH distribution (wt%)	Variance of the WEH distribution	χ^2 for Pearson criteria	p-level for Pearson criteria
Reference distribution		81	831	5467	2.54 ± 0.02	0.33	—	—
Phyllosilicates		5	51	293	2.57 ± 0.07	0.27	1.55	0.908
Monohydrated sulfates		4	45	307	2.41 ± 0.09	0.33	7.74	0.257
Polyhydrated sulfates	All	10	101	638	2.78 ± 0.05	0.25	24.30	0.0005
	Of "high intensity"	5	50	312	2.88 ± 0.07	0.24	21.79	0.0006
	Of "low intensity"	5	51	326	2.68 ± 0.07	0.24	7.81	0.252

Table 2: Comparison of parameters of WEH distributions for groups of CRISM pixels. WEH is derived from the DAN passive data for the case of short-range variability of AEC mass fraction (SR case).

Groups of CRISM pixels		Coverage of the traverse (%)	Number of CRISM pixels	Number of DAN measurements	Mean of the WEH distribution (wt%)	Variance of the WEH distribution	χ^2 for Pearson criteria	p-level for Pearson criteria
Reference distribution		81	831	5467	2.64 ± 0.02	0.30	—	—
Phyllosilicates		5	51	293	2.57 ± 0.06	0.17	18.46	0.001
Monohydrated sulfates		4	45	307	2.37 ± 0.09	0.33	11.04	0.051
Polyhydrated sulfates	All	10	101	638	3.06 ± 0.06	0.31	129.22	3.48×10^{-26}
	Of "high intensity"	5	50	312	3.10 ± 0.06	0.18	72.74	5.99×10^{-15}
	Of "low intensity"	5	51	326	2.75 ± 0.05	0.14	9.33	0.156

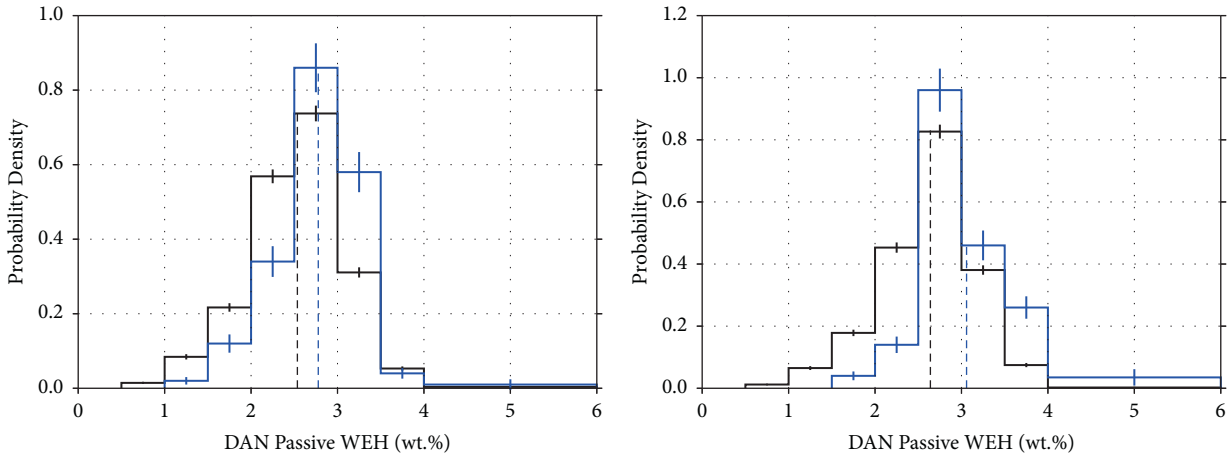

Figure 2: Distributions of the WEH values according to (a) LR approach and (b) SR approach for AEC estimations along the Curiosity traverse. The black line shows WEH distribution for the reference group of the CRISM pixels, which do not have signatures of hydrated minerals. The blue line represents the WEH distribution for the group of CRISM pixels with the spectral signature of polyhydrated sulfates. Dotted lines indicate the mean WEH values of the distributions.

neutron emission. Instead of the WEH value, we used the ratio of the count rates of total C_{CTN} and epithermal C_{CETN} neutrons emitted by the surface, namely, $F_{DAN} = C_{CTN}/C_{CETN}$ (for more details, see [16]). The results of the performed analysis are described in Table 3. The relationship between the parameters of the F_{DAN} distributions is found to be similar to the same parameters of the WEH distributions (Tables 1 and 2). Only the distribution of F_{DAN} for the testing group of CRISM pixels associated with the presence of polyhydrated sulfates is confidently different from the reference distribution of F_{DAN} for the group of pixels, which do not have the spectral signature of hydrated minerals. So, one

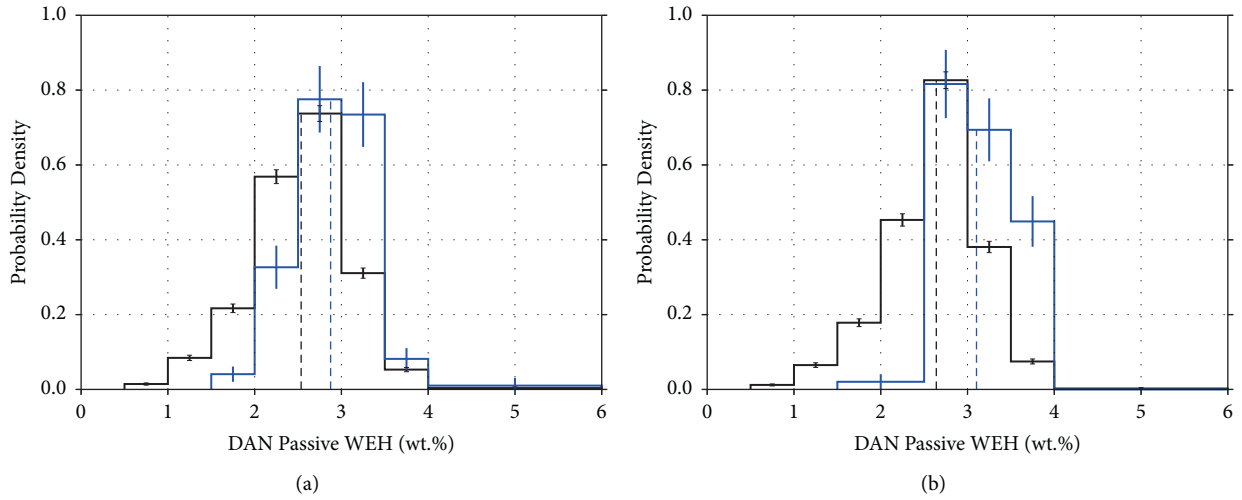

Figure 3: Same as for Figure 2, but the blue line represents the WEH distribution for the group of CRISM pixels with the "high intensity" spectral signature of polyhydrated sulfates.

Table 3: Comparison of parameters of F_{DAN} distributions for groups of CRISM pixels.

Groups of CRISM pixels		Coverage of the traverse (%)	Number of CRISM pixels	Number of DAN measurements	Mean of the F_{DAN} distribution	Variance of the F_{DAN} distribution	χ^2 for Pearson criteria	p-level for Pearson criteria
Reference distribution		81	831	5467	3.20 ± 0.02	0.26	—	—
Phyllosilicates		5	51	293	3.13 ± 0.05	0.14	7.74	0.052
Monohydrated sulfates		4	45	307	2.95 ± 0.08	0.28	11.12	0.049
Polyhydrated sulfates	All	10	101	638	3.47 ± 0.04	0.16	34.56	5.71×10^{-7}
	Of "high intensity"	5	50	312	3.63 ± 0.06	0.16	53.69	1.31×10^{-11}
	Of "low intensity"	5	51	326	3.31 ± 0.05	0.12	8.70	0.034

had to conclude that the relationship found between the presence of polyhydrated sulfates and increase of water in the shallow subsurface is not produced by WEH deconvolution procedure, but manifests physical relation between such minerals and neutron emission.

5. Discussion

Thus, the conclusion should be drawn that, along the traverse from the landing site to the distance mark of about 20 km, the presence of polyhydrated sulfates on the surface, as observed by CRISM, is consistent with the increase of WEH values within a subsurface layer of about 60 cm thickness, as measured by DAN. On the other hand, no such phenomenon is found for another group of CRISM pixels associated with the spectral signatures of phyllosilicates or monohydrated sulfates. One may speculate that the part of the traverse, which manifests the phenomenon of CRISM-DAN cross-correspondence, is associated with the sedimentary strata containing polyhydrated sulfates probably with significant thickness that leads to enhanced mass fraction of water in comparison with the "usual" subsurface with some standard mass fraction of water. The top surfaces of such matter are observable by CRISM from the Martian orbit and their deeper volumes are detectable by DAN from the Martian surface. One suggests naming such strata as layers of polyhydrated sulfates-rich matter, or PHSR matter.

To test this simplest interpretation of the found phenomenon, one might check the possibility that the observed WEH distribution in the area with PHSR matter (Figure 2) could be modeled by a bimodal function with two distinct components: the "less-WEH" component and "more-WEH" component (Figure 4). The "less-WEH" component could be associated with the "usual" matter. Its shape could be taken from the known distribution of WEH for the reference group of CRISM pixels with no signatures of any of the three types of hydrated minerals (Figure 2). The mean values for WEH of this component are known to be equal to (2.54 ± 0.02) wt% for the LR approach and (2.40 ± 0.02) wt% for the SR approach (see Table 1). The "more-WEH" component could be associated with polyhydrated sulfates. As the simplest option, this "more-WEH" component could be represented by a normal distribution with two free parameters: the mean value and the sample variance.

Using such a bimodal model, one may try to fit the observed WEH distribution in the area of CRISM pixels with a spectral signature of polyhydrated sulfates. In addition to the two free parameters of the "more-WEH" component, one more parameter should be used for fitting: the relative fraction α of this component with respect to the total integral

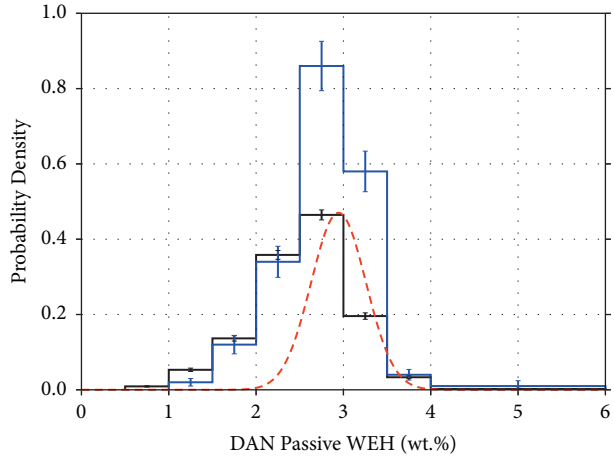

Figure 4: The bimodal distribution of WEH for the pixels with the spectral signature of polyhydrated sulfates (blue line): the more-WEH component of the distribution (dotted red line) represents the surface, dominated by polyhydrated sulfates, the less-WEH component of the distribution (black line) is the reference distribution taken with its modelled contribution.

of the entire observed distribution. Two cases of the observed distributions are tested for WEH derived by either LR or SR approaches of DAN passive data processing. One-tailed Pearson's chi-squared test is applied for finding the best fitting parameters of the bimodal model (Table 4).

In both cases, for LR and SR approaches, the Pearson criteria give very good p-level values for consistency between the observed distribution and the modeling function; i.e., it is between 0.001 and 0.15 (Table 4). The "more-WEH" component has the mean WEH values equal to 3.0 or 3.6 wt % for the cases of LR and SR, respectively (Table 4 and Figure 2).

Taking into account this result, one may speculate that the two components of WEH distribution represent two fractions of PHSR matter. The "less-WEH" component corresponds to the "usual" soil and the "more-WEH" component might be attributed to deposits of polyhydrated sulfates. The bimodal approximation of the observed WEH distribution for the area of PHSR matter allows determining the fraction parameter α for the contribution of "more-WEH" component. This fraction is about 0.37 or 0.12 (as a part of 1) of the entire WEH distributions, based on either LR or SR approaches, respectively. In the case of the proposed identification, such a fraction α corresponds to the part of the subsurface volume, which contains deposits of polyhydrated sulfates with the thickness large enough for neutron sensing. Another fraction $(1-\alpha)$ corresponds to the "usual" soil. Interestingly, the fraction of the "more-WEH" component is approaching the value of 1 for the subgroup of 51 pixels of "high intensity" spectral signature of polyhydrated sulfates (Table 4). It is another piece of evidence for the identification of "more-WEH" component in the areas, the substances of which is the deposition of polyhydrated sulfates.

The fraction of "usual" soil in the PHSR matter might exist practically everywhere along the traverse. This substance does not contain noticeable quantities of any of the three types of hydrated minerals and has an average WEH of about 2.5 wt% (see Tables 1 and 2). The WEH value for this second fraction of PHSR matter corresponds to the number of water molecules in the structure of polyhydrated sulfates. Its value was derived from the DAN data, as about 3 wt% (Table 4). The chemically bound water of hydrated minerals was embedded in their structure long time ago, when these minerals were formed in the aqueous conditions. Therefore, the type of PHS-dominated substance is thought to contain the "initial water" of Mars.

The mass fraction of polyhydrated sulfates in the subsurface substance may vary along the traverse. At some spots with the most intense spectral signatures of polyhydrated sulfates, the "more-WEH" component, as shown above, may contribute the observed WEH distribution entirely. One may use the DAN passive data for testing the presence of polyhydrated sulfates in the subsurface along the traverse with the spatial resolution about hundreds meters or so.

For performing such test we split the total path of about 20 km into 132 distance intervals of 150 meters long, each including around 50 passive measurements of WEH with a spatial resolution of 3 meters. The distribution of the WEH values for each distance interval is tested by the already known bimodal function with only one variable parameter α, as the fractionation of the already known components of "less-water" and "more-water," α and $1-\alpha$, respectively. The best fitting value of α could be considered as the average mass fraction of polyhydrated sulfates in the subsurface. Performing such an analysis for all 132 distance intervals, one obtains the profile of the polyhydrated sulfates mass fraction along the traverse (Figure 5).

The profile shows that the highest value of α equal to 0.21 (the confidence is 15%) is observed at the area around a distance mark of 16,300 m. Indeed, according to the CRISM data, this area is characterized by the increased value of the spectral signature brightness for polyhydrated sulfates (Figure 6). Thus, the analysis of the DAN passive data made it possible to identify sites with an increased content of polyhydrated sulfates in the shallow subsurface. One of such sites is found at the distance mark of 16,300 meters of the traverse on the way from Bagnold Dunes to Vera Rubin ridge.

Table 4: Best fitting parameters of bimodal model for WEH distribution for the group of CRISM pixels with the signature of polyhydrated sulfates (cases of LR and SR are presented for estimations of WEH from the DAN passive data).

Distributions of WEH for CRISM pixels along the rover traverse		Fraction of the component of bimodal model representing polyhydrated sulfates (in parts of 1)	Parameters of the normal distribution of WEH for the component of bimodal model representing polyhydrated sulfates		χ^2 minimum value	p-level
			Mean (wt %)	Variance		
Polyhydrated sulfates	According to the LR case	0.37 (+0.11/−0.10)	3.00	0.24	6.75	0.150
Polyhydrated sulfates of "high intensity"		0.99 (+0.01/−0.64)	2.87	0.43	8.78	0.032
Polyhydrated sulfates	According to the SR case	0.12 (+0.01/−0.01)	3.59	0.19	17.29	0.001
Polyhydrated sulfates of "high intensity"		1.00 (+0.00/−0.21)	3.13	0.22	5.64	0.060

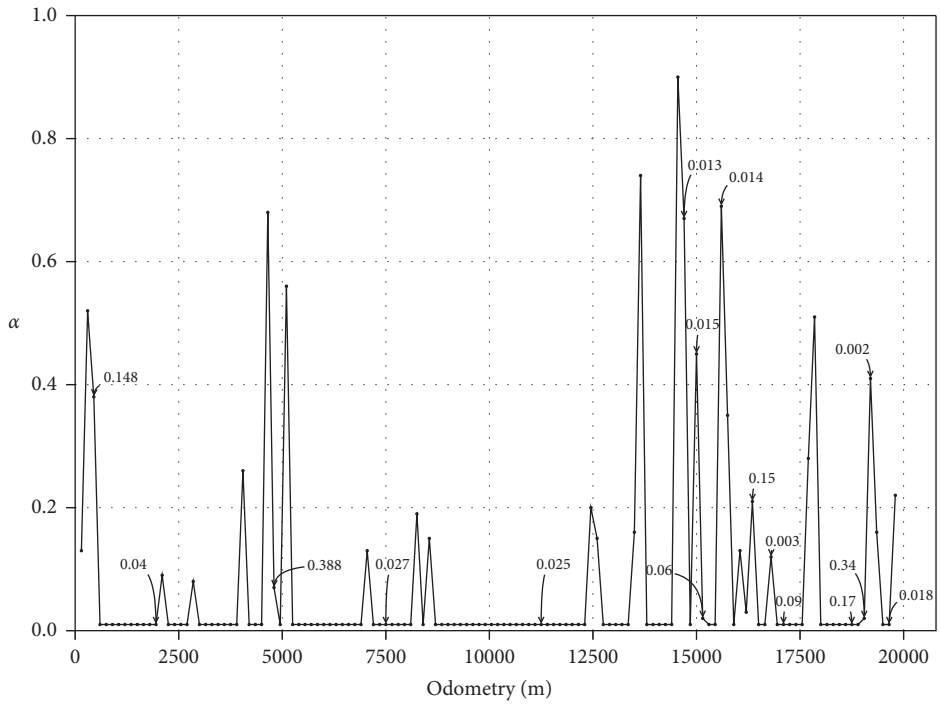

Figure 5: The distance profile of the polyhydrated sulfates mass fraction (α) along the traverse. The captions correspond to the significant probabilities of α.

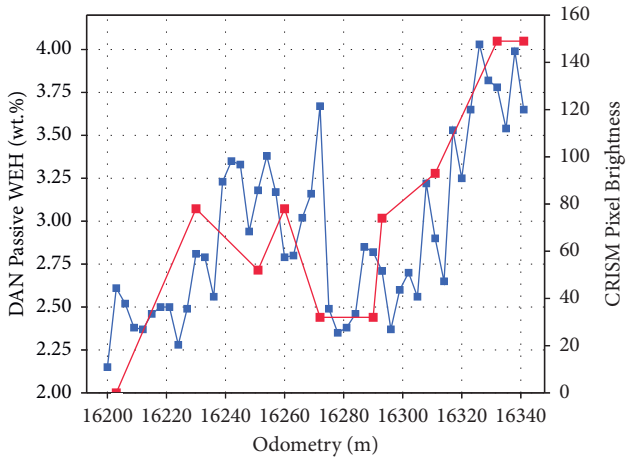

FIGURE 6: The distance profile of the DAN passive measurements of WEH with spatial resolution of 3 m (blue line) and the pixel brightness corresponding to polyhydrated sulfates according to CRISM specialized browse product mosaics (red line) for the distance interval of 16,200–16,350 m. The dotted line shows the mean WEH value for the whole traverse.

6. Conclusions

The cross-analysis of the WEH values from the DAN passive measurements onboard Curiosity and Specialized Browse Product Mosaics of CRISM spectrometer onboard the MRO was performed for the part of the rover traverse from the landing site up to the distance mark 19 971 m. It was found that traverse intervals with the spectral signature of polyhydrated sulfates, as detected by CRISM, contain more WEH in the subsurface in comparison with the intervals that do not manifest signatures of any of the three selected types of hydrated minerals, such as phyllosilicates and mono- and polyhydrated sulfates. This effect points out that polyhydrated sulfates exist at some places along the traverse, as layers with up to 60 cm thickness that are well detectable by DAN with its sensing depth of about 60 cm in the subsurface.

The bimodal distribution of WEH was found for such distance intervals along the traverse with the spectral signature of polyhydrated sulfates. The "less-WEH" component of this distribution is consistent with the distribution observed at the dominating majority of distance intervals that do not manifest any spectral signatures of all three tested types of hydrated minerals. The average water content for this type of matter is 2.5 wt%. The "more-WEH" component of this distribution is thought to be associated with the second type of matter, whose composition is likely dominated by polyhydrated sulfates component. The value of WEH for this type is about 3 wt% or larger.

The absence of any difference between WEH distributions for the distance intervals without spectral signatures of the three tested types of hydrated minerals and for distance intervals with spectral signatures of phyllosilicates and monohydrated sulfates does not necessarily make a discrepancy between CRISM and DAN observations. Indeed, the uppermost layer of the subsurface with such hydrated minerals may be seen by CRISM, but might be too thin for the detection by DAN. One may suspect that for some reason the top layers with polyhydrated sulfates are thick enough for being detected by DAN, while the top layers of phyllosilicates and monohydrated sulfates are not.

The CRISM pixels with the spectral signature of polyhydrated sulfates cover about 10% of the 20 km long rover traverse that was analyzed. The fact of the large thickness of polyhydrated sulfates deposits suggests a long period of time in the past, when such layer had enough time to be accumulated. On the other hand, the areas of CRISM pixels with spectral signatures of phyllosilicates and monohydrated sulfates are most likely associated with rather thin layers on top of the ordinary rocks and soil. DAN is not sensitive to the presence of such thin layers on top of the ordinary matter. One may expect that the presence of such hydrated minerals will also be proved by cross-analysis of CRISM and DAN data, when the rover climbs up Aeolis Mons, where the deposits if phyllosilicates or monohydrated sulfates might be thick enough for the detection of the WEH increase contributed by them.

Data Availability

Data from this work are publicly accessible on the Planetary Data System, https://www.pds.nasa.gov/.

Disclosure

This paper was presented at EGU General Assembly 2020 [22].

Conflicts of Interest

The authors declare that they have no conflicts of interest.

Acknowledgments

This work was funded by the Ministry of Science and Higher Education of the Russian Federation, "Exploration" theme grant AAAA-A18-118012290370-6. The authors highly appreciate the excellent support of the DAN investigation from the Curiosity project team.

References

[1] B. J. Thomson, N. T. Bridges, R. Milliken et al., "Constraints on the origin and evolution of the layered mound in Gale Crater, Mars using Mars Reconnaissance Orbiter data," *Icarus*, vol. 214, no. 2, pp. 413–432, 2011.

[2] N. A. Cabrol, E. A. Grin, H. E. Newsom, R. Landheim, and C. P. McKay, "Hydrogeologic evolution of gale crater and its relevance to the exobiological exploration of mars," *Icarus*, vol. 139, no. 2, pp. 235–245, 1999.

[3] S. Clifford and T. J. Parker, "The evolution of the martian hydrosphere: implications for the fate of a primordial ocean and the current state of the northern plains," *Icarus*, vol. 154, no. 1, pp. 40–79, 2001.

[4] O. Abramov and D. A. Kring, "Impact-induced hydrothermal activity on early Mars," *Journal of Geophysical Research*, vol. 110, Article ID E12S09, 2005.

[5] S. P. Schwenzer, O. Abramov, C. C. Allen et al., "Gale crater: formation and post-impact hydrous environments," *Planetary and Space Science*, vol. 70, no. 1, pp. 84–95, 2012.

[6] J. P. Grotzinger, S. Gupta, M. C. Malin et al., "Deposition, exhumation, and paleoclimate of an ancient lake deposit, gale crater, mars," *Science*, vol. 350, no. 6257, Article ID aac7575, 2015.

[7] R. Y. Sheppard, R. E. Milliken, M. Parente, and Y. Itoh, "Updated perspectives and hypotheses on the mineralogy of lower Mt. Sharp, Mars, as seen from orbit," *Journal of Geophysical Research: Planets*, vol. 126, no. 2, Article ID e2020JE006372, 2021.

[8] R. E. Milliken, J. P. Grotzinger, and B. J. Thomson, "Paleoclimate of mars as captured by the stratigraphic record in gale crater," *Geophysical Research Letters*, vol. 37, Article ID L04201, 2010.

[9] E. B. Rampe, D. F. Blake, T. F. Bristow et al., "Mineralogy and geochemistry of sedimentary rocks and eolian sediments in gale crater, mars: a review after six earth years of exploration with curiosity," *Geochemistry*, vol. 80, no. 2, Article ID 125605, 2020.

[10] J. P. Grotzinger and R. E. Milliken, "The sedimentary rock record of Mars: distribution, origins, and global stratigraphy," *SEPM Special Publications*, vol. 102, pp. 1–48, 2012.

[11] J.-P. Bibring, Y. Langevin, J. F. Mustard et al., "Global mineralogical and aqueous mars history derived from OMEGA/mars express data," *Science*, vol. 312, no. 5772, pp. 400–404, 2006.

[12] G. M. Martínez, E. Fischera, N. O. Rennó et al., "Likely frost events at Gale crater: analysis from MSL/REMS measurements," *Icarus*, vol. 280, pp. 93–102, 2016.

[13] D. I. Lisov, M. L. Litvak, A. S. Kozyrev, I. G. Mitrofanov, and A. B. Sanin, "Data processing results for the active neutron measurements by the DAN instrument on the curiosity mars rover," *Astronomy Letters*, vol. 44, no. 7, pp. 482–489, 2018.

[14] M. L. Litvak, I. G. Mitrofanov, A. B. Sanin et al., "Local variations of bulk hydrogen and chlorine-equivalent neutron absorption content measured at the contact between the sheepbed and Gillespie Lake units in Yellowknife Bay, gale crater, using the DAN instrument onboard curiosity," *Journal of Geophysical Research: Planets*, vol. 119, no. 6, pp. 1259–1275, 2014.

[15] I. G. Mitrofanov, M. L. Litvak, A. B. Varenikov et al., "Dynamic albedo of neutrons (DAN) experiment onboard NASA's mars science laboratory," *Mars Science Laboratory*, vol. 170, no. 1–4, pp. 559–582, 2012.

[16] S. Y. Nikiforov, I. G. Mitrofanov, M. L. Litvak et al., "Assessment of water content in martian subsurface along the traverse of the curiosity rover based on passive measurements of the DAN instrument," *Icarus*, vol. 346, Article ID 113818, 2020.

[17] A. B. Sanin, I. G. Mitrofanov, M. L. Litvak et al., "Data processing of the active neutron experiment DAN for a Martian regolith investigation," *Nuclear Instruments and Methods in Physics Research Section A: Accelerators, Spectrometers, Detectors and Associated Equipment*, vol. 789, pp. 114–127, 2015.

[18] J. Bell, Ed., *The Martian Surface. Composition, Mineralogy and Physical Properties*, Cambridge University Press, Cambridge, NY, USA, 2008.

[19] I. G. Mitrofanov, M. L. Litvak, A. B. Sanin et al., "Water and chlorine content in the Martian soil along the first 1900 m of the curiosity rover traverse as estimated by the DAN instrument," *Journal of Geophysical Research*, vol. 119, no. 7, pp. 1579–1596, 2014.

[20] S. Murchie, R. Arvidson, P. Bedini et al., "Compact reconnaissance imaging spectrometer for mars (CRISM) on mars reconnaissance orbiter (MRO)," *Journal of Geophysical Research*, vol. 112, no. E5, 2007.

[21] CRISM, "Description of specialized browse product mosaics," 2020, http://crism.jhuapl.edu/msl_landing_sites/index_news.php.

[22] M. Djachkova, I. Mitrofanov, M. Litvak, D. Lisov, S. Nikiforov, and A. Sanin, "Testing correspondence between areas with hydrated minerals, as observed by CRISM onboard MRO, and spots of enhanced subsurface water content, as found by DAN along the traverse of curiosity," *EGU General Assembly*, Article ID EGU2020-9993, 2020.

Hindawi
Advances in Astronomy
Volume 2021, Article ID 6441233, 11 pages
https://doi.org/10.1155/2021/6441233

Research Article

Brine-Induced Tribocorrosion Accelerates Wear on Stainless Steel: Implications for Mars Exploration

Javier Martín-Torres,[1,2] **María-Paz Zorzano-Mier**,[1,3] **Erik Nyberg**,[4] **Abhilash Vakkada-Ramachandran**,[4] **and Anshuman Bhardwaj**[1]

[1]*Department of Planetary Sciences, School of Geosciences, University of Aberdeen, King's College, Aberdeen AB24 3UE, UK*
[2]*Instituto Andaluz de Ciencias de La Tierra (CSIC-UGR), Granada, Spain*
[3]*Centro de Astrobiología (INTA-CSIC), Madrid, Spain*
[4]*Department of Computer Science, Electrical and Space Engineering, Luleå University of Technology, Luleå, Sweden*

Correspondence should be addressed to Javier Martín-Torres; javier.martin-torres@abdn.ac.uk

Received 1 June 2021; Revised 22 November 2021; Accepted 13 December 2021; Published 28 December 2021

Academic Editor: Yu Liu

Tribocorrosion is a degradation phenomenon of material surfaces subjected to the combined action of mechanical loading and corrosion attack caused by the environment. Although corrosive chemical species such as materials like chloride atoms, chlorides, and perchlorates have been detected on the Martian surface, there is a lack of studies of its impact on materials for landed spacecraft and structures that will support surface operations on Mars. Here, we present a series of experiments on the stainless-steel material of the ExoMars 2020 Rosalind Franklin rover wheels. We show how tribocorrosion induced by brines accelerates wear on the materials of the wheels. Our results do not compromise the nominal ExoMars mission but have implications for future long-term surface operations in support of future human exploration or extended robotic missions on Mars.

1. Introduction

Tribocorrosion is a surface damage phenomenon resulting from the synergistic action of mechanical wear and (electro) chemical reactions. It can imply corrosion accelerated by wear, or wear accelerated by chemical reactions [1]. It was discovered in 1875 by Thomas Edison, who observed a variation in the coefficient of friction between metal and chalk moistened with electrolyte solutions [2], and today it is an important engineering topic, defined by ISO [3] and ASTM [4], and a cause for concern to any engineer employing passive metal components in corrosive environments [5]. If adequately controlled, tribocorrosion can be beneficial, such as in machinery lubricants where it is used as a means of avoiding seizure by promoting wear in a sacrificial mode [6]. Sacrificial mode is a concept in lubrication technology that is used to avoid seizure of mechanical components. Wear is promoted to reduce friction. This can be achieved by incorporating sulphur or chlorine via chemical additives in oil. Under conditions of wear, chlorine or sulphur reacts with nascent metal exposed by wear to produce iron chloride, which is weaker than the original steel.

The surface of Mars is rich in corrosive chemical species. Martian regolith contains abundant chloride [7] which forms various chlorides and perchlorate salts with high solubilities and low eutectic temperatures [8, 9]. Detection of 0.4–0.6% perchlorate by mass in Martian high latitudes and further revelation of soluble chemistry of Martian soil at the Phoenix Lander site [10] were encouraging results prompting researchers to focus on perchlorate-based brine research. Other remaining anions and cations, as detected by the Wet Chemistry Laboratory on the Phoenix Mars Lander, were chloride, bicarbonate, and sulphate and Mg^{2+}, Na^{+}, K^{+}, and Ca^{2+}, respectively [10]. Subsequently, the reanalysis of the Viking results also suggested the plausible presence of perchlorate and organics at midlatitudes on Mars [11], as well as theoretical modelling at the landing site of InSight

[12]. Evidence for sodium perchlorate ($NaClO_4$), magnesium perchlorate ($Mg(ClO_4)_2$), and calcium perchlorate ($Ca(ClO_4)_2$) has also been provided (with specific phases of the perchlorates not being determined yet) at equatorial latitudes by the Sample Analysis at Mars instrument on the Mars Science Laboratory (MSL) [13]. Another study [14] provides evidence of Martian perchlorate, chlorate, and nitrate in the Martian meteorite EETA79001 with sufficiently high concentrations. These results indicate the possibility that perchlorates might be abundantly present within Martian regolith at all latitudes. A variety of pathways have been proposed for the perchlorate synthesis on Mars. These pathways may involve photochemical reactions [15], electrostatic discharge [16], and oxidation-reduction reactions [17]. Perchlorates and chloride salts in the Martian regolith are extensively investigated because they can absorb water from the atmosphere forming hydrates [18], by absorption, and then liquid brines, through deliquescence [19, 20]. In addition to perchlorates, chlorides such as $FeCl_3$, $CaCl_2$, and $MgCl_2$ can also act as strong freezing point depressants. $FeCl_3$ and $CaCl_2$ are the strongest freezing point depressants with eutectic temperatures as low as approximately 218 K, followed by $MgCl_2$, NaCl, and KCl at about 238 K, 252 K, and 262 K, respectively [9].

Perchlorates (ClO_4^-) have been found planet-wide on Mars [10]. Studies show that the perchlorate salts which contain ClO_4^- anion can hold the water in brine state even when the temperature reaches 203 K. Other chloride (Cl^-) salts have been detected such as magnesium chloride ($MgCl_2$) and calcium chloride ($CaCl_2$) [21], along with sulphate salts such as iron sulphate [22], which has deliquescent properties. Of course, the eutectic temperature of perchlorate is affected by cations, and not all chlorates have equally low eutectic temperatures.

A recent work [23] has derived the current chemical weathering rates on Mars, based on the oxidation of iron in stony meteorites investigated by the Mars Exploration Rover Opportunity at Meridiani Planum. The authors concluded that the chemical weathering rates derived are ~1 to 4 orders of magnitude slower than that of similar meteorites found in Antarctica where the slowest rates are observed on Earth, suggesting that aridity of Mars is even more significant than expected during the last 50 Myr. The authors extrapolated their results to the impact of weathering in the wheels of the NASA Curiosity rover, pointing out that Martín-Torres et al. [19] "worry that the corrosive effects of chlorine brine might pose a challenge to the rover. The extremely slow weathering of meteorites, which contain metallic iron as a phase very sensitive towards chemical alteration, suggests that this is not a threat over the lifetime of a spacecraft, however. The Opportunity rover is testament to that, showing no signs of chemical weathering or corrosion after more than 12 years of operating on Mars (April 2016)."

The argument used by Schroeder et al. (2016) to justify the absence of corrosion on mechanical parts on Mars actually supports the hypothesis that environmental conditions have an impact on the fate of the rover wheels. The wheels of Opportunity and Curiosity were similar in terms of composition and effective ground pressure supported (see Materials and Methods). The fact that Opportunity showed no signs of chemical weathering or corrosion after more than 14 Earth years of operation on Mars (from 2004 until the middle of 2018), while Curiosity rover faced extreme corrosion and related punctures and tears just months after landing on Mars, maybe an indication of the impact of the local environment on wheels weathering. Actually, the details of this wear and tear on the wheels of Curiosity rover are missing from Schröder et al. [23].

Corrosion of the surface of a metal is the degradation that results from its chemical interaction with the environment. On Mars, any metal facing the sky, as the observable side of a meteorite, would only be exposed to the air, and thus only ambient oxygen would produce this damage. This is the case analysed by Schroeder et al. (2016), which considers only the chemical weathering rates of metals exposed to the Martian atmosphere. However, in the case of metals in contact with the regolith, as it is the case of the metals used in the wheels of the rovers operating on Mars, these materials may be eventually directly exposed to Cl and potential brines, which are formed naturally under Martian conditions at the interface of the regolith and the atmosphere [18–20]. These two processes are very different, as in the case of the wheels, in addition to the exposure to a liquid phase, there is the additional damage of mechanical wearing. It is known that metal can be protected from corrosion by covering it with a coating, such as an anodised treatment; however, as soon as this protective layer is scratched or worn out, the inner material is directly exposed to corrosion. Curiosity's wheel is made from a single piece of machined aluminium alloy AA7075-T7351. The main rim is 1.9 cm thick (0.75 inches) [23]. Martín-Torres et al. [19] hypothesised that the daily contact of the wheels with the corrosive perchlorate solutions during every night may have weakened the scratched surface of the anodised aluminium, making it more susceptible to damage against sharp rocks. Although the large cracks observed in the wheels of Curiosity are likely caused by mechanical damage, an image taken by the ChemCam Remote Microscopic Imager on Sol 502 in the vertical wall of the T-print of the wheels, showed a pattern of distributed submillimetre sized blisters that cannot be attributed to rock scratching and resembled aluminium alloy pitting corrosion [24]. Unfortunately, the Spirit and Opportunity rovers did not have an equivalent camera to analyse the wheels with submillimetre precision, so we cannot state whether this damage existed or not.

Previous preliminary experiments, designed to look at the interaction between aerospace aluminium alloy (AA7075-T73) and the gases present in the Mars atmosphere, at 20°C and a pressure of 700 Pa with only 0.13% of oxygen, showed that there is an interaction between the small amount of oxygen present in the Mars gas and the alloy, when there is a scratch that removes the protective aluminium oxide film [25]. The anodising process that is applied to aluminium alloy increases the thickness of the natural oxide layer on the aluminium wheels, but the abrasion can wear out the external protecting layer and expose the bare aluminium metal to corrosion. The purpose of this work is to evaluate the role of direct contact with

liquid brines and the additional damage caused by mechanical friction.

Here, we present laboratory studies that show the impact of tribocorrosion (the combination of mechanical and corrosion wearing) on materials in contact with naturally formed brines under current environmental conditions on Mars. Although tribocorrosion is a well-known phenomenon since nearly 150 years ago, there is a lack of analysis of its impact on materials for landed spacecraft and structures that will support surface operations on Mars. Mechanical parts, like the wheels of the rovers operating on Mars, in contact with corrosive brines on the surface, could be affected by the combination of chemical corrosion and mechanical loading. Nevertheless, to our knowledge, no single research on tribocorrosion research on Mars has ever been published, even though corrosive materials have been found on the surface of Mars.

The European Space Agency ExoMars 2022 Rosalind Franklin rover will have a nominal lifetime of 218 sols (around 7 Earth months). Its mass is 310 kg, with an instrument payload of 26 kg (excluding payload servicing equipment such as the drill and sample processing mechanisms). The rover's kinematic configuration is based on a six-wheel, triple-bogie concept with locomotion formula $6 \cdot 6 \cdot 6 + 6$, denoting six supporting wheels, six driven wheels, and six steered wheels, plus six articulated (deployment) knee drives. This system enables the rover to passively adapt to rough terrains, providing inherent platform stability without the need for a central differential [26]. The wheels are made of Sandvik stainless spring steel 11R51 (https://www.materials.sandvik/en/materials-center/material-datasheets/strip-steel/sandvik-11r51/).

Here, we have performed laboratory studies on how the material (stainless spring steel) used in ExoMars 2022 Rosalind Franklin rover wheels is affected first by corrosion and then by tribocorrosion under environmental conditions on Mars. We suggest that similar studies should be conducted on other materials used for wheels and structures in contact with the Martian regolith.

2. Materials and Methods

2.1. Brine Corrosion under Martian Conditions. For the study of corrosion, we have tested samples of the Sandvik 11R51 stainless steel, used in the ExoMars 2022 Rosalind Franklin rover wheels, and two other control materials: stainless steel SS4301 and regular steel S235. Sandvik 11R51 is austenitic (US and Euro standards: AISI 301, EN 1.4310) stainless steel with excellent spring properties with higher corrosion resistance (due to the addition of molybdenum), mechanical strength, tensile strength and tempering effect, and fatigue and relaxation properties. Every material was exposed to two sets of salt environments inside the SpaceQ chamber at Martian conditions [27] (260 K and 6 mbar) and three control tests with salt (see Table 1) under ambient laboratory conditions (293 K and 1010 mbar). To simulate the Martian conditions, the chamber was first vacuumed and filled with pure CO_2 gas till it reached 6 mbar. Then, water was injected to create water vapour in the atmosphere till RH reached 40%, then the liquid nitrogen (LN_2) was allowed to flow through the cooling plate which reached a temperature of 260 K, and then temperature was allowed to slowly increase to ambient lab conditions due to the thermal equilibrium.

Cases #1 and #2 were exposed for 5 hours to the Martian environment within the SpaceQ chamber, and to the simulated Martian water cycle described in Materials and Methods. The set of control samples #1, #2, and #3 were left on the bench at laboratory conditions during the same time, and the control sample #1 was immersed in a brine of $NaClO_4$ (1.5 g salt + 1 g water) to observe the reactiveness of the material within the liquid already formed. After the experiments, the samples were packed in an airtight bag and studied using a scanning electron microscope (SEM) along with elemental detection via electron dispersive X-ray spectroscopy (EDS) to determine the effects of corrosion. The samples were only temporarily stored for transport in the airtight bag, and the clean metal was exposed during SEM.

The overview of the optical inspection by digital microscopy is shown in Table 2. We found no corrosion on either of the stainless-steel samples (11R51 or SS4301). On the contrary, the regular steel sample (Reg S235) presented visible signs of corrosion, both in Case #1 (simulating Mars environment and immersed in the brine that is formed spontaneously by absorption of the moisture in the air) and in Case #2 (simulating Mars environment and immersed in soil + salt), whereas the same immersion under ambient atmosphere produced less corrosion (Control #2). This was qualitatively determined based on optical inspection with microscope. Examples are shown in Table 2. It is worth pointing out that these brines are formed spontaneously and are stable transiently at nighttime Martian surface conditions, depending on the season and local environmental conditions [19].

In order to identify spectrally the corrosion in S235 under Case #1, we performed the analysis with the SEM-EDS as seen in Figures 1(a)–1(c). The digital microscope image in (a) shows clear visible signs of corrosion. A region that included corroded and noncorroded steel was selected for high magnification studies (green box). In (b), four regions along a vertical line were selected for EDS analysis. The EDS spectra in (c) show that regions related to spectra 3 and 4 are enriched in carbon (C at 0.27 keV), oxygen (O at 0.52 keV), and sodium (Na at 1.04 keV) compared to the reference regions in spectra 1 and 2. These results are evidence of oxidation of the regular steel by the sodium perchlorate brine. Interestingly, carbon and oxygen, from the Martian atmosphere and the water in the brine and air, have also been fixed with different efficiencies from spectrum 1 to spectrum 4, depending on the redox state of the material after the corrosion.

Actually, it is worth remarking that upon exposure to two different environments (Earth and Mars environments), the regular steel was more severely corroded under Martian conditions (Cases #1 and #2) than under ambient conditions (see for comparison Case #2 vs. Control# 2 in Table 2), so the corrosion of regular steel S235 is amplified under Martian conditions relatively to those on Earth. The brines were effectively formed under Martian conditions because of the high relative humidity conditions (40% RH), whereas at ambient conditions in

Table 1: Environmental conditions of the experiments performed with 11R51, SS4301, and S235.

Case	Conditions	Salt environments
#1	SpaceQ Martian conditions (pressure = 6 mbar; temperature = 260 K)	1.5 g $NaClO_4$ (+water spontaneously absorbed from the atmosphere)
#2	SpaceQ Martian conditions (pressure = 6 mbar; temperature = 260 K)	1.5 g MMS soil + 0.15 g $NaClO_4$ salt (+water spontaneously absorbed from the atmosphere)
Control #1	Laboratory conditions	$NaClO_4$ (1.5 g salt + 1 g water) brine immersion
Control #2	Laboratory conditions	1.5 g MMS soil + 0.15 g $NaClO_4$ salt
Control #3	Laboratory conditions	Indoors (exposed to the air at ambient lab conditions)

Table 2: Optical inspection of the experiments.

Condition	Sandvik 11R51	SS4301	Reg S235
Case #1 (SpaceQ brine)	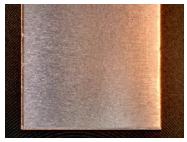 No corrosion	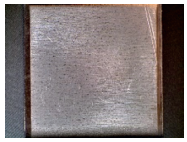 No corrosion	 Severe corrosion
Case # 2 (SpaceQ soil + salt)	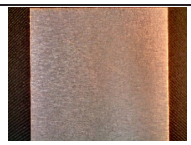 No corrosion	 No corrosion	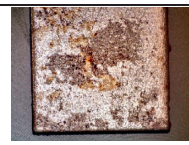 Severe corrosion
Control 1 (ambient brine)	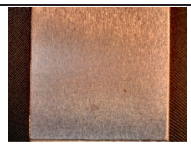 No corrosion	 No corrosion	N/A Insufficient samples. Severe corrosion expected
Control 2 (ambient soil + salt)	 No corrosion	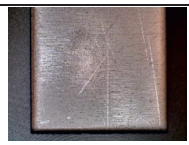 No corrosion	 Corrosion
Control 3 (ambient)	 No corrosion	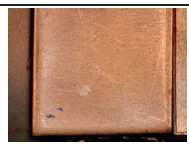 No corrosion	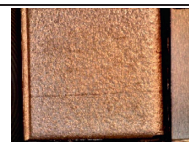 No corrosion

the laboratory the relative humidity was moderated (10% RH).

2.2. Tribocorrosion under Martian Conditions. As shown in Table 2, the material used in the ExoMars wheels (stainless spring steel Sandvik 11R51) showed no corrosion under static corrosion experiments, neither on Earth nor under Martian conditions. We have conducted a tribological experiment to evaluate if it is feasible to corrode (oxidise) stainless steel when subjected to wear while exposed to a liquid brine of the type that can be formed under Martian conditions. The experiment was conducted by rubbing for 90 minutes a 10 mm ceramic (Si_3N_4) ball against the material, while the plate was immersed in either brine or water (see Figure 2 for the setup). This is a standard procedure for testing tribocorrosion.

For the analysis we included the following (see Supplementary Materials): (i) measurements of friction during rubbing; (ii) wear volume by 3D optical profilometer; (iii) optical inspection with digital microscope; and (iv) scanning electron microscopy and electron dispersive X-ray spectroscopy (SEM-EDS) for detailed surface analysis including chemical (elemental) analysis.

Figure 3 shows the friction data and shows a clear difference between testing in water and brine. The friction coefficient is initially increasing to values above 1, but for the wear test in brine the friction drops significantly after 30 min (1800 s). The drop in friction could be explained by the

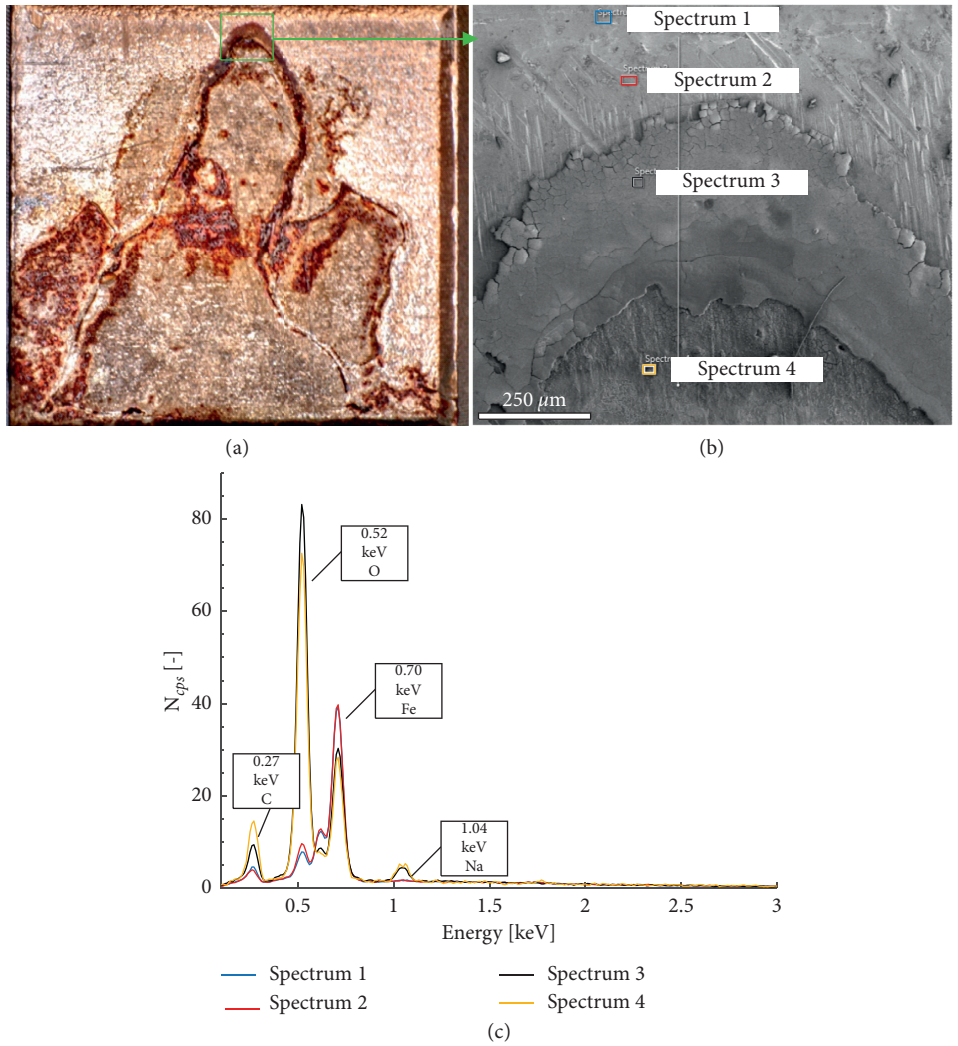

Figure 1: (a) Microscope image of 10 × 10 mm regular steel sample. (b) High magnification SEM image showing location of EDS analysed regions. (c) Results of EDS analysis confirming corrosion by detection of Na and O in spectra 3 and 4.

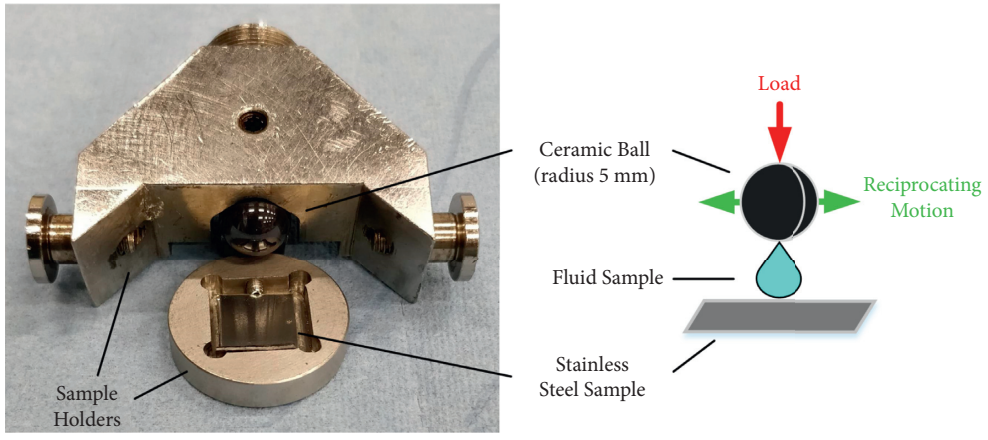

Figure 2: Setup of tribological experiment showing ceramic ball and stainless-steel plate in their respective sample holders.

chemical reactions that reduce the surface integrity and thereby lower friction. In tribology, this is known as sacrificial wear and is commonly employed in the antiseizure chemical additives known as extreme pressure agents (EP). They are used in extreme pressure gear lubrication, and they function by promoting wear so that friction is reduced. Chlorine containing EP agents has historically been used but is not recommended as it may cause corrosion [28].

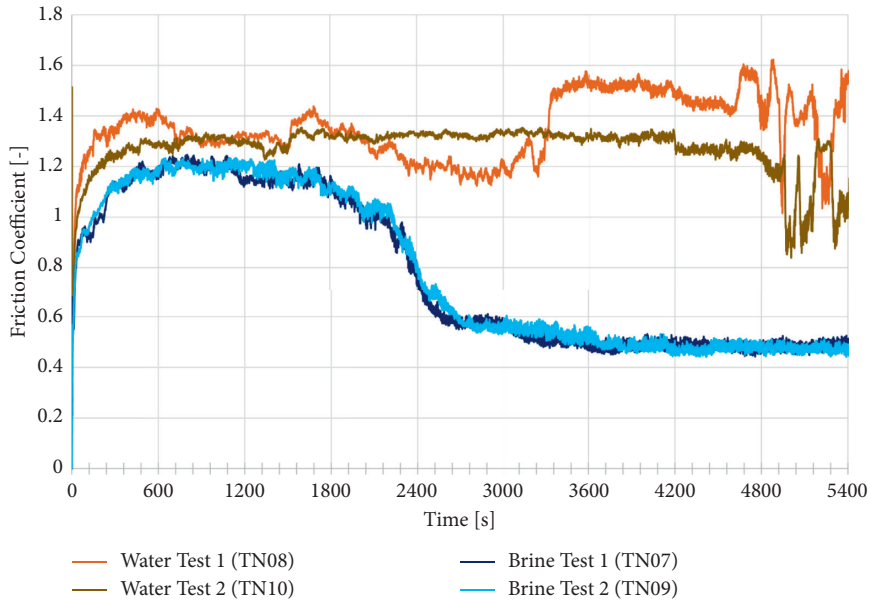

Figure 3: Friction data indicates transition to corrosive wear around time of 1800 s when immersed in brine.

Table 3: Wear data.

	Worn volume (μm^3)	Max depth (μm)	Projected area (mm^2)	Worn volume per cycle (μm^3)
TN07 brine	80 466 771	41.2	3.16	1490
TN08 water	54 217 302	38.4	3.59	1004
TN09 brine	78 590 249	40.5	3.19	1455
TN10 water	26 081 611	19.6	3.53	483

Table 3 shows that the worn volume is significantly increased (>45%) when the test is performed in brine instead of water. TN10 has the lowest worn volume of all samples, indicating that brines have >45% worn volume in these experiments.

The wear marks are shown in Figure 4 after washing the samples in two steps in heptane and ethanol in ultrasonic bath. The samples tested in water show a visual appearance that could be interpreted as corrosion, while the samples tested in brine are brighter in appearance except along the edges. The repeatability is good. Figure 5 shows an overview of the reference samples at low and high magnification and shows tests TN08 and TN07 (water and brine respectively). The edges of the wear marks were selected for further analysis. Figure 6 shows detection of Cl in worn area of TN07 (brine); Figure 7 shows evidence of surface oxidation but no detection of Cl in worn area of TN08 (water); and Figure 8 shows, as expected, no signals of Cl, as test was run in deionised water. In this case, surface appears to be oxidised and is rich in Si (likely from ceramic Si3N4 ball).

The results shown in Figures 4–8 can be summarised as follows: (i) a solution of 50/50 wt% $NaClO_4$ to H_2O promotes wear when increasing the wear volume by over 45% in the tribological test; (ii) friction is significantly reduced by brine, compared with water; (iii) chlorine is detected in the wear track (<3 at%); and (iv) friction and wear data, combined with chemical analysis, indicate that in comparison to water, the brine favours a sacrificial wear mechanism, meaning that friction is reduced at the expense of higher wear.

3. Results and Discussion

The main conclusion of these experiments is that brine accelerates wear by chemical reaction leading to a sacrificial wear mechanism. In the sacrificial wear mechanism, Cl reacts with the steel surface (Fe) to reduce the toughness of the surface material. The consequence is that the resulting metal can wear more easily than the original did. This is a well-known concept in tribology—it is the basic principle relied on in antiseizure (also called extreme pressure) additives—where it is sometimes necessary to sacrifice material to reduce friction.

The experiments clearly demonstrate that wear under briny conditions result in a combination of a damaged passive layer and the presence of chlorides, which are the two factors usually associated with an increased risk of pitting corrosion. The duration of the presented experiment was about 5 hours, which is much shorter than the lifetime of the rovers on Mars. It can reasonably be assumed that the rovers' wheels, after a long exposition to the surface and Martian atmosphere, may get damaged. In that case, an oxide layer damaged by wear will not

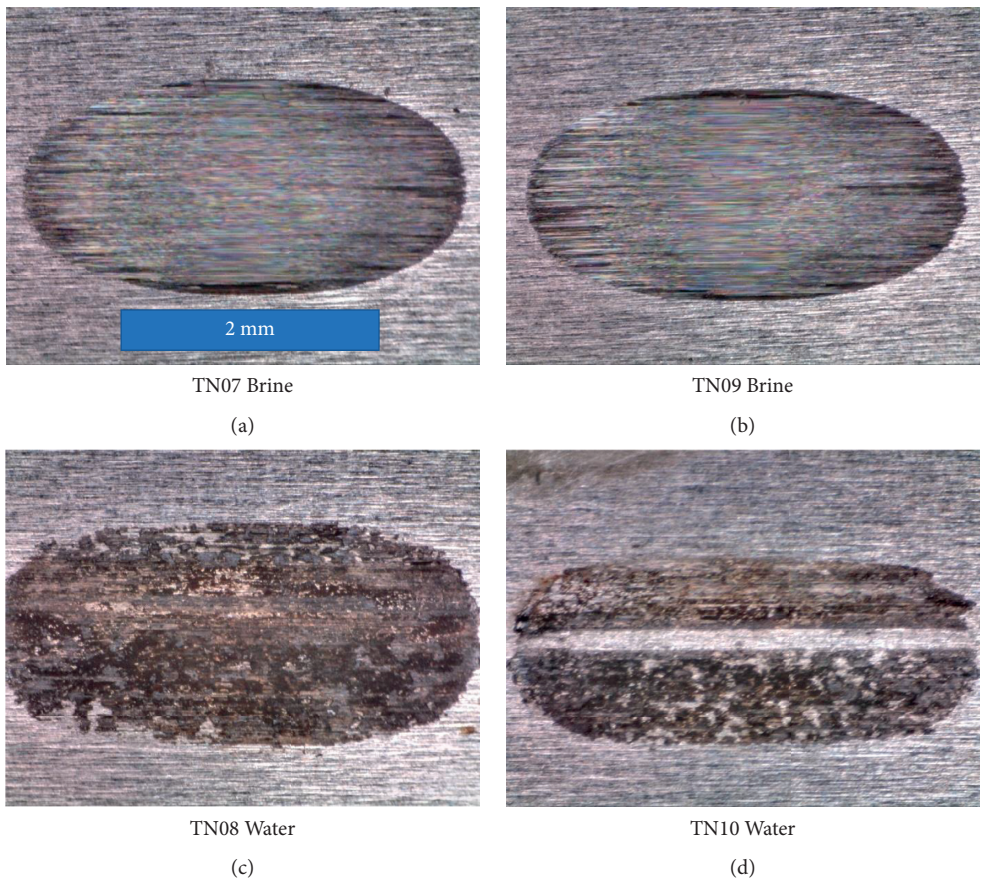

Figure 4: Friction data (scale shown in (a)). (a) TN07 brine. (b) TN09 brine. (c) TN08 water. (d) TN10 water.

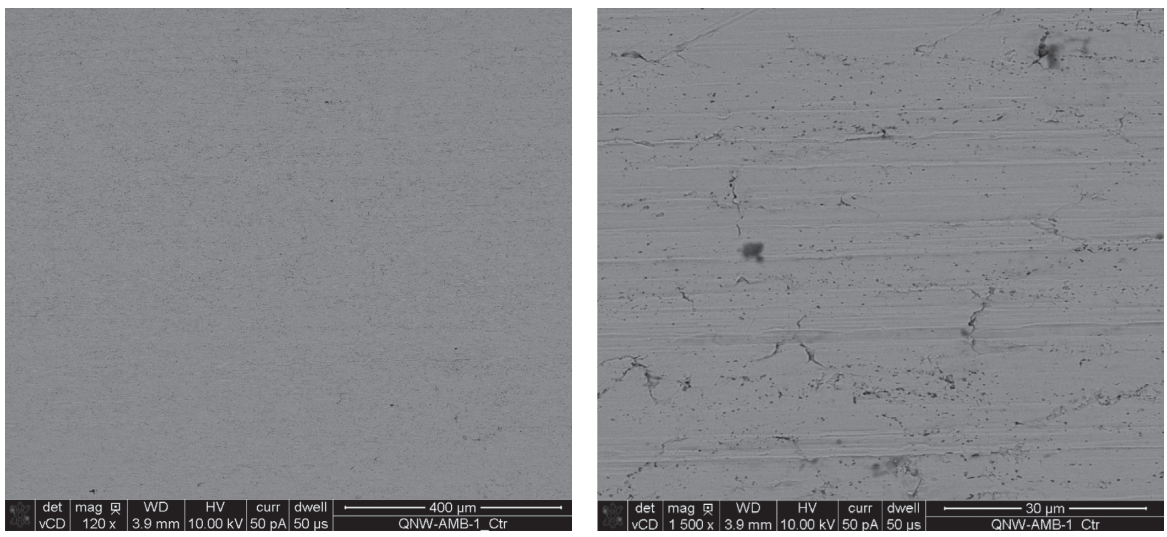

(a) (b)

Figure 5: Continued.

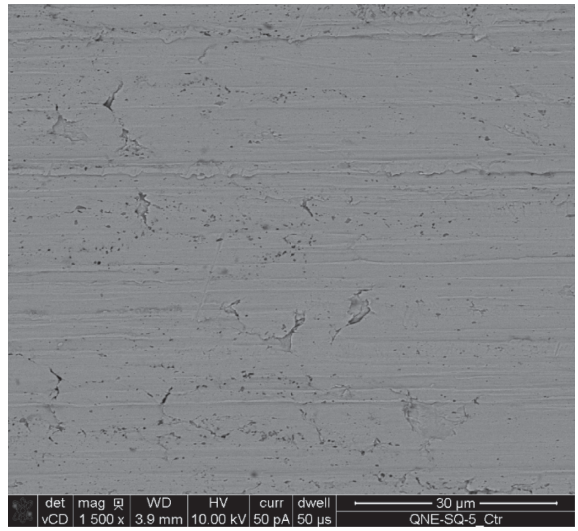

(c)

Figure 5: Reference samples (scale shown in the figures). (a) Reference sample 1 (ambient conditions) at low magnification. (b) Reference sample 1 (ambient) at high magnification. (c) Reference sample 2 (SpaceQ brine) at high magnification.

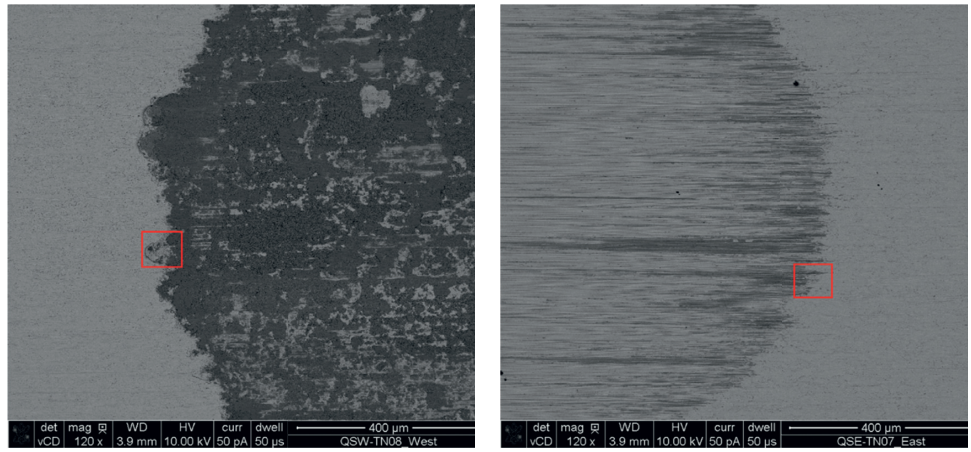

(a) (b)

Figure 6: SEM overview of experiments: (a) TN08 (water). (b) TN07 (brine).

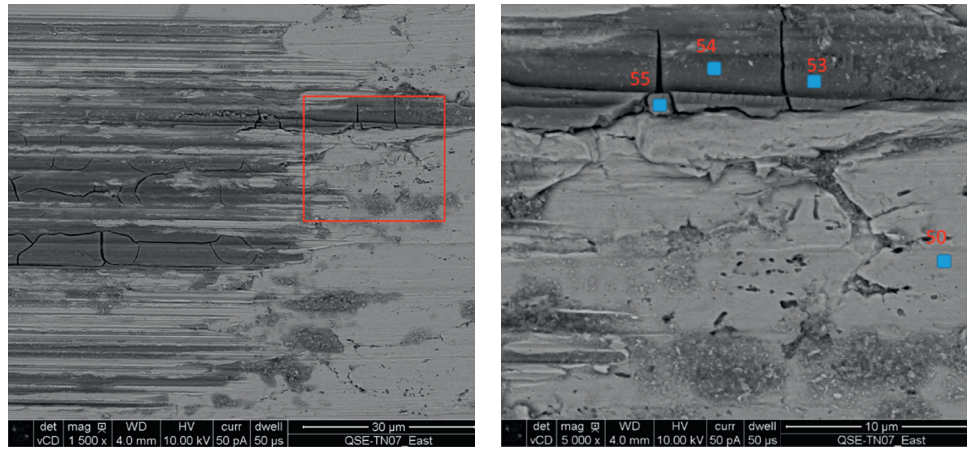

TN07 Brine, Edge of Wear Mark TN07 Brine High Magnification

(a) (b)

Figure 7: Continued.

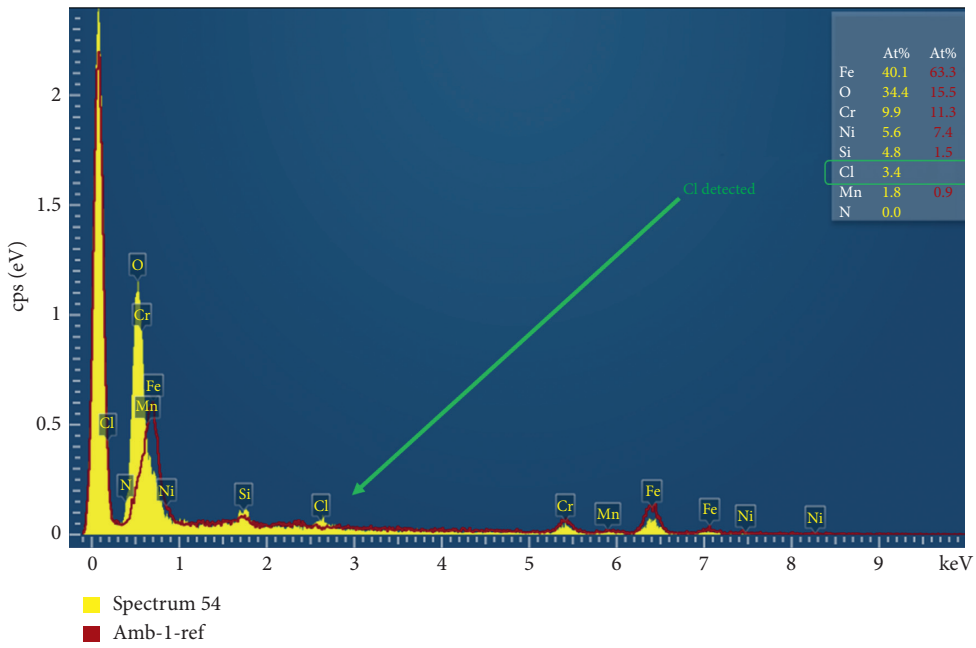

(c)

Figure 7: Detection of Cl in test with brine. (a) TN07 brine, edge of wear mark. (b) TN07 brine, high magnification.

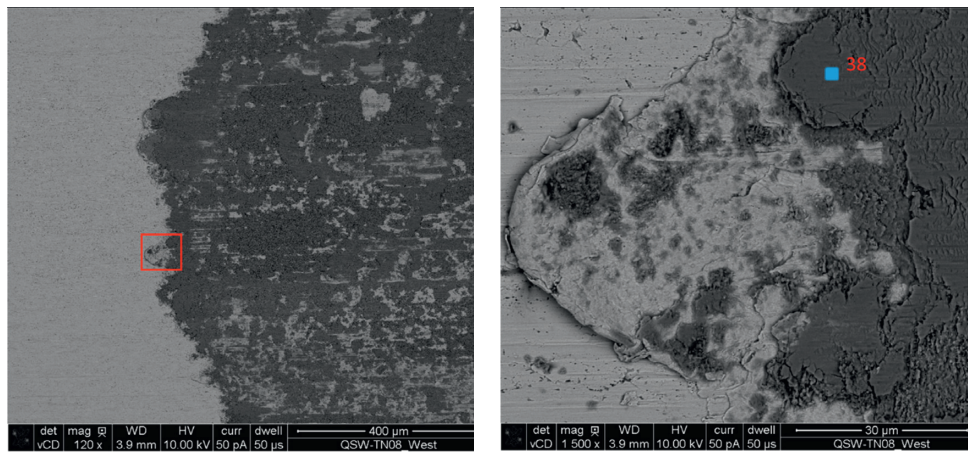

TN08 Water, Edge of Wear Mark

(a)

TN08 Water High Magnification

(b)

Figure 8: Continued.

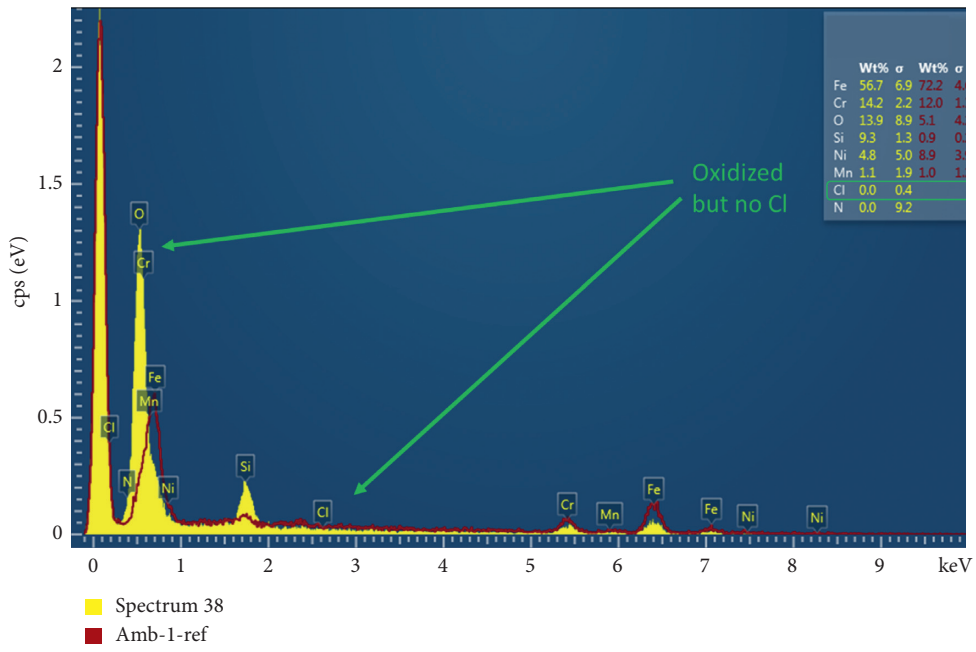

Figure 8: No Cl detected from water test. (a) TN08 water, edge of wear mark. (b) TN08 water, high magnification.

regenerate, due to the lack of available oxygen. Additionally, the experiments presented here are a conservative case (low corrosion case) of the real conditions of Mars, as other perchlorates, like MgClO4 and CaClO4, are the main perchlorates present on Mars [29].

From the surface analysis (SEM-EDS), it was clear that Cl was present in the steel surface material after the wear process in brine, and therefore the corrosion risk should be further investigated.

Although the materials used in Mars exploration may be resistant to chemical corrosion from brines in static conditions, mechanical wear only has to remove a few nanometres of oxide to accelerate the corrosion [30]. Tribocorrosion should not be overlooked in selecting materials or special protective treatments for landed spacecraft and structures that will support surface long-term operations for the human exploration of Mars, and in particular for the wheels of the Martian rovers that will operate for long term in the harsh conditions of Mars.

Further studies are needed to consider other important components of the Mars surface environment that can affect this interaction, such as the effect of oxidants, the effect of radiation on their oxidising properties, the possible catalytic effects of the minerals present in the Martian regolith, the diurnal thermal changes, and variation in ambient humidity, and in particular to develop more detailed studies including all the perchlorates existing on the surface of Mars to quantity the impact of tribocorrosion. Once on Mars, it would be useful to perform regular monitoring of the wheels with the robotic arm camera of the rovers. That would allow to observe and characterise the impact of tribocorrosion and also to infer the occurrence of brines on Mars.

Data Availability

All the data are available in the main text or the supplementary materials.

Disclosure

This manuscript has been uploaded to the open server of Research Square: https://www.researchsquare.com/article/rs-36280/v1.

Conflicts of Interest

The authors declare that they have no known competing financial interests or personal relationships that could have appeared to influence the work reported in this paper.

Authors' Contributions

JMT was responsible for conceptualisation, supervision, investigation, writing the original draft, funding acquisition, and resources. MPZ contributed to conceptualisation, methodology, supervision, investigation, writing the original draft, and funding acquisition. EN carried out the tribocorrosion and corrosion experiments and reviewed and edited the manuscript. AVR conducted the corrosion experiments; provided experimental support to the tribocorrosion experiments; and reviewed and edited the manuscript. AB reviewed and edited the manuscript.

Acknowledgments

The authors thank the ExoMars Project Team, European Space Agency (ESA), for reviewing the manuscript. The SpaceQ chamber has been developed in collaboration with Kurt J. Lesker Company and was funded by the Kempe Foundation. MPZ's contribution has been partially supported by the Spanish State Research Agency (AEI), Project No. MDM-2017-0737, Unidad de Excelencia "María de Maeztu"–Centro de Astrobiología (CSIC-INTA).

Supplementary Materials

The Supplementary Materials contain a detailed explanation of the steps followed in the brine corrosion and tribocorrosion tests and how the water and temperature cycle in the Martian near-surface have been performed. As complementary information, we give an estimate of the effective ground pressure of the Curiosity, Spirit, and Opportunity rovers. . (*Supplementary Materials*)

References

[1] S. W. Watson, F. J. Friedersdorf, B. W. Madsen, and S. D. Cramer, "Methods of measuring wear-corrosion synergism," *Wear*, vol. 181-183, pp. 476–484, 1995.

[2] T. Edison, *Improvement in Telegraph Apparatus*, 1875.

[3] International Organization for Standardization, *International Organization for, S. Corrosion of Metals and Alloys – Vocabulary (ISO 8044:2020)*, International Organization for Standardization, Geneva, Switzerland, 2020.

[4] *American Society for, T. & Materials*, 2017.

[5] D. Landolt and S. Mischler, *Tribocorrosion of Passive Metals and Coatings*, Woodhead Publishing Limited, Sawaton, UK, 2011.

[6] G. W. Rowe, "The chemistry of tribology, friction, lubrication and wear," *Royal Institute of Chemistry Reviews*, vol. 1, no. 2, pp. 135–204, 1968.

[7] A. Bhardwaj, L. Sam, F. J. Martín-Torres, and M. P. Zorzano, "Are slope streaks indicative of global-scale Aqueous processes on contemporary Mars?" *Reviews of Geophysics*, vol. 57, no. 1, pp. 48–77, 2019.

[8] A. Bhardwaj, L. Sam, F. J. Martín-Torres, M.-P. Zorzano, and R. M. Fonseca, "Martian slope streaks as plausible indicators of transient water activity," *Scientific Reports*, vol. 7, no. 1, p. 7074, 2017.

[9] B. Clark and D. van Hart, "The salts of Mars," *Icarus*, vol. 45, no. 2, pp. 370–378, 1981.

[10] M. H. Hecht, S. P. Kounaves, R. C. Quinn et al., "Detection of perchlorate and the soluble chemistry of martian soil at the Phoenix lander site," *Science*, vol. 325, no. 5936, pp. 64–67, 2009.

[11] R. Navarro-González, E. Vargas, J. de la Rosa, A. C. Raga, and C. P. McKay, "Reanalysis of the Viking results suggests perchlorate and organics at midlatitudes on Mars," *Journal of Geophysical Research*, vol. 115, no. E12, 2010.

[12] P. Bernadett and Á. Kereszturi, "Annual and daily ideal periods for deliquescence at the landing site of InSight based on GCM model calculations," *Icarus*, vol. 340, Article ID 113639, 2020.

[13] D. P. Glavin, C. Freissinet, K. E. Miller et al., "Evidence for perchlorates and the origin of chlorinated hydrocarbons detected by SAM at the Rocknest aeolian deposit in Gale Crater," *Journal of Geophysical Research: Planets*, vol. 118, no. 10, pp. 1955–1973, 2013.

[14] S. P. Kounaves, B. L. Carrier, G. D. O'Neil, S. T. Stroble, and M. W. Claire, "Evidence of martian perchlorate, chlorate, and nitrate in Mars meteorite EETA79001: implications for oxidants and organics," *Icarus*, vol. 229, pp. 206–213, 2014.

[15] D. C. Catling, M. W. Claire, K. J. Zahnle et al., "Atmospheric origins of perchlorate on Mars and in the atacama," *Journal of Geophysical Research*, vol. 115, 2010.

[16] K. Tennakone, "Contact electrification of regolith particles and chloride electrolysis: synthesis of perchlorates on Mars," *Astrobiology*, vol. 16, no. 10, pp. 811–816, 2016.

[17] B. L. Carrier and S. P. Kounaves, "The origins of perchlorate in the Martian soil," *Geophysical Research Letters*, vol. 42, no. 10, pp. 3739–3745, 2015.

[18] L. Ojha, M. B. Wilhelm, S. L. Murchie et al., "Spectral evidence for hydrated salts in recurring slope lineae on Mars," *Nature Geoscience*, vol. 8, no. 11, pp. 829–832, 2015.

[19] F. J. Martín-Torres, M.-P. Zorzano, P. Valentín-Serrano et al., "Transient liquid water and water activity at Gale crater on Mars," *Nature Geoscience*, vol. 8, no. 5, pp. 357–361, 2015.

[20] E. G. Rivera-Valentín, V. F. Chevrier, A. Soto, and G. Martínez, "Distribution and habitability of (meta)stable brines on present-day Mars," *Nature Astronomy*, vol. 4, no. 8, pp. 756–761, 2020.

[21] M. M. Osterloo, F. S. Anderson, V. E. Hamilton, and B. M. Hynek, "Geologic context of proposed chloride-bearing materials on Mars," *Journal of Geophysical Research*, vol. 115, no. E10, 2010.

[22] V. F. Chevrier and T. S. Altheide, "Low temperature aqueous ferric sulfate solutions on the surface of Mars," *Geophysical Research Letters*, vol. 35, no. 22, 2008.

[23] C. Schröder, P. A. Bland, M. P. Golombek, J. W. Ashley, N. H. Warner, and J. A. Grant, "Amazonian chemical weathering rate derived from stony meteorite finds at Meridiani Planum on Mars," *Nature Communications*, vol. 7, no. 1, p. 13459, 2016.

[24] C. Vargel, *Corrosium of Aluminium*, 2004.

[25] L. M. Calle, W. Li, M. R. Johansen, J. W. Buhrow, and C. I. Calle, *Corrosion on Mars: An Investigation under Relevant Simulated Martian Environments*, 2017.

[26] J. L. Vago, F. Westall, A. J. Coates et al., "Habitability on early Mars and the search for biosignatures with the ExoMars rover," *Astrobiology*, vol. 17, no. 6-7, pp. 471–510, 2017.

[27] A. Vakkada Ramachandran, M. I. Nazarious, T. Mathanlal, M.-P. Zorzano, and J. Martín-Torres, "Space environmental chamber for planetary studies," *Sensors*, vol. 20, no. 14, p. 3996, 2020.

[28] L. R. Rudnick, *Lubricant Additives : Chemistry and Application*, CRC Press, Florida, FL, USA, 2003.

[29] S. Civiš, A. Knížek, P. B. Rimmer et al., "Formation of methane and (Per)Chlorates on Mars," *ACS Earth and Space Chemistry*, vol. 3, no. 2, pp. 221–232, 2019.

[30] L. M. Calle, *Corrosion on Mars: Effect of the Mars Environment on Spacecraft Materials*, 2019.

Hindawi
Advances in Astronomy
Volume 2021, Article ID 9924571, 10 pages
https://doi.org/10.1155/2021/9924571

Research Article

Subsurface Thermal Modeling of Oxia Planum, Landing Site of ExoMars 2022

M. Formisano,[1] **M. C. De Sanctis**,[1] **C. Federico**,[1] **G. Magni**,[1] **F. Altieri**,[1] **E. Ammannito**,[2] **S. De Angelis**,[1] **M. Ferrari**,[1] **and A. Frigeri**[1]

[1]*INAF-IAPS, Via del Fosso del Cavaliere 100, Rome, Italy*
[2]*Italian Space Agency (ASI), Rome, Italy*

Correspondence should be addressed to M. Formisano; michelangelo.formisano@inaf.it

Received 8 March 2021; Revised 18 May 2021; Accepted 25 June 2021; Published 2 September 2021

Academic Editor: Eriita Jones

Numerical simulations are required to thermophysically characterize Oxia Planum, the landing site of the mission ExoMars 2022. A drilling system is installed on the ExoMars rover, and it will be able to analyze down to 2 meters in the subsurface of Mars. The spectrometer Ma_MISS (Mars Multispectral Imager for Subsurface, Coradini and Da Pieve, 2001) will investigate the lateral wall of the borehole generated by the drill, providing hyperspectral images. It is not fully clear if water ice can be found in the subsurface at Oxia Planum. However, Ma_MISS has the capability to characterize and map the presence of possible ices, in particular water ice. We performed simulations of the subsurface temperatures by varying the thermal inertia, and we quantified the effects of self-heating. Moreover, we quantified the heat released by the drilling operations, by exploring different frictional coefficients and angular drill velocities, in order to evaluate the lifetime of possible water ice.

1. Introduction

The target of the ExoMars 2022 mission is to investigate an ancient location with high potential for past habitability or for chemical biosignatures—indicators of extant life—as well as abiotic/prebiotic organics [1–3]. This location has been identified in Oxia Planum, a 200 km-wide low-relief terrain [4], at a latitude of about 18°. Oxia Planum shows evidence of subaqueous episodes being characterized by hydrous clay-bearing bedrock units and layered outcrops [4–6]. The entire area of Oxia is undergoing erosion, attested by morphology (inverted features) and crater statistics [4]. This site is also important for the complex environment reconstruction (see, for example, [7]). Moreover, the surface rocks of Oxia are less exposed to oxidation and radiation compared with other sites since they have been exposed by the cosmic bombardment only recently [3, 4].

The drilling system onboard the ExoMars rover will be able to penetrate down to 2 meters in the subsurface of Oxia Planum [3, 8]. The main aim of the drill is to acquire subsurface samples with high astrobiological potential to be delivered to the analytical lab for a detailed investigation, but before the sample extraction, the sample context is analyzed by Ma_MISS (Mars Multispectral Imager for Subsurface) that will observe the lateral wall of the borehole generated by the drill, with the production of hyperspectral images [9, 10]. Ma_MISS will provide information about the mineralogy, oxidation state, and hydration state of the sample before the extraction and crushing of the sample, an important aspect since deep cold samples may be altered by the drilling activity and also after their extraction. Moreover, Ma_MISS has been validated by laboratory tests [9, 11], and it can infer information on grain size using the analysis of specific spectral parameters. Also, another ExoMars instrument, such as Close-Up Imager (CLUPI) [12] can give information of the fines that drill will extract.

Buried ice in the subsurface is not expected at the Oxia Planum landing site; however, recent results from the Fine-Resolution Epithermal Neutron Detector (FREND) instrument on board Trace Gas Orbiter (TGO) have pointed out the presence of ice permafrost oases near the Martian equator [13]. It is important to understand the thermal state

of the subsurface at Oxia Planum and the influence of the drilling activity. The characterization and the mapping of the organic and volatile content in the subsurface have a great scientific impact [14]: therefore, numerical simulations are required to produce, for example, maps of temperature of the surface/subsurface of Oxia Planum. Also, evaluating the heat contribution released by the drilling system, we will establish if hypothetical water ice in the subsurface could be preserved or not [15, 16], having in mind that the low atmospheric pressure on Mars leads to very fast sublimation of any ice-rich deposit in direct contact with the drill tip [3].

The estimation of the thermal inertia of Oxia Planum is a matter of debate. In [17], a high-resolution map of thermal inertia derived from the observations of planetary brightness temperature by the Mars Global Surveyor (MGS) Thermal Emission Spectrometer (TES) is presented; in that work, Oxia Planum exhibits thermal inertia between 300 and 400 thermal inertia units, hereafter TIU. Jones et al. [18] suggested a thermal inertia of about 260 TIU, interpreting the surface as consisting of dark fines, with some coarse sand and duricrust but very little dust, with grain size below 3 mm. However, in [4], for the clay-bearing unit, thermal inertia in the range of 550–650 TIU was reported, and this probably represents the likely landing site; river delta, instead, is characterized by a low thermal inertia (<100 TIU). Finally, in [19], the clay unit is characterized by a thermal inertia of 370–380 TIU while the river delta by a value of 300 TIU.

In this work, from a thermophysical point of view, we characterized the landing site Oxia Planum. In particular, we investigated firstly the thermal response of the subsurface to different thermal inertia values, taking into account the considerations discussed above and after we evaluated the heat released by the drilling operations. We also estimated the lifetime of a hypothetical icy subsurface deposit. The paper is structured as follows: in Section 2, we report the numerical model adopted in this work, in Section 3, the results obtained by the numerical simulations are given, and finally, in Section 4, the discussion and the conclusion are given.

2. Numerical Model

We performed our simulations using a 3D finite element code (e.g., [24–28]), which solves the classical heat equation in a parallelepiped (see Figure 1) compatible with the dimension of a borehole, generated by the drilling system, installed on the ExoMars rover, in Oxia Planum.

The top (x-y plane) of this domain is modeled with a Gaussian random surface in order to simulate the roughness of the surface. The dimensions of the domain are 1 cm × 1 cm × 50 cm. A depth of 50 cm has been chosen since the diurnal skin depth is reasonably of the order of tens of centimeters and also compatible with the length of a rod of the drill onboard ExoMars [29].

We solve the following equation:

$$\rho c_p \frac{\partial T}{\partial t} = K\vec{\nabla} \cdot (\vec{\nabla} T), \tag{1}$$

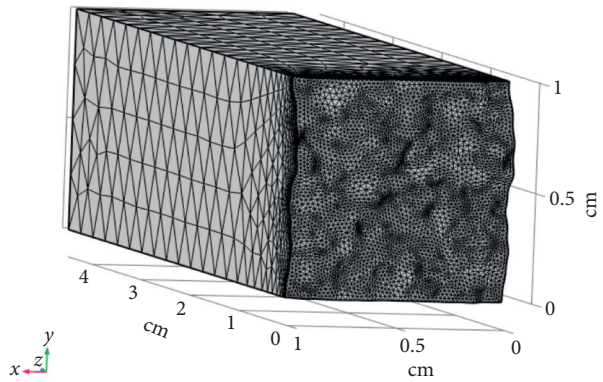

Figure 1: Domain of integration for the first part of this work: zoom of the first 5 cm from the Martian surface. A radiation boundary condition is imposed at the top (x-y plane), while zero flux is applied on the other sides.

where T is the temperature, t the time, ρ the density, c_p the specific heat, and K the thermal conductivity. Heat transfer occurs only by conduction since convection is negligible due to the small temperature gradients involved as well as the characteristic size of the sample. At the top, we imposed a radiation boundary condition, while on the other sides, zero heat flux is imposed.

In particular at the top, following, e.g., [30, 31], we solve for each facet

$$S_c(1-a)\cos(Z) + Q_{SH} = -K\vec{n} \cdot \vec{\nabla} T + \varepsilon\sigma T^4, \tag{2}$$

where S_c is the solar constant (scaled for Mars' heliocentric distance) in Wm^{-2}, a is the albedo, $\cos(Z)$ is the cosine of the solar incidence, ε is the emissivity, and σ is the Stefan–Boltzmann constant. The illumination conditions (i.e., $\cos(Z)$) are calculated according to [24, 26, 28]. As in [26], we consider a diffuse surface, which absorbs the solar irradiation and emitted IR radiation as a grey body with an emissivity of 0.97, an approach similar to [32]. The term Q_{SH} is the term related to the so-called "self-heating."

The initial temperature is set at 200 K, which is compatible with the surface equilibrium temperature.

We developed three different models, characterized by different thermal inertia: model A, characterized by $I = 160$ TIU; model B characterized by $I = 255$ TIU; and model C characterized by $I = 650$ TIU. Models A and B are characterized by a thermal conductivity of 0.018 $\mathrm{Wm}^{-1}\mathrm{K}^{-1}$ and 0.048 $\mathrm{Wm}^{-1}\mathrm{K}^{-1}$, respectively. These values are compatible with those provided by the InSight mission [22]; the density, in these cases, is low and set at 1700 kgm^{-3}, which corresponds to a high-porous sedimentary rock [21]. Model C is characterized by a high thermal conductivity of 0.2 $\mathrm{Wm}^{-1}\mathrm{K}^{-1}$ and a density typical of the clay, i.e., 2700 kgm^{-3} [23]. In all the models, the specific heat is set at 800 $\mathrm{J\,kg}^{-1}\mathrm{K}^{-1}$, which is a value compatible with many materials (i.e., regolith, fine sand, and coarse sand, e.g., [20]). The albedo is 0.13 [18].

The heliocentric distance explored is the aphelion since the landing is currently planned for June 10, 2023, while Mars is very close to its aphelion.

All the thermophysical parameters used in this work are listed in Table 1.

3. Results

We start the discussion about the results of part I, i.e., the influence of the thermal inertia on the subsurface temperatures of Oxia Planum, evaluating also the effects of self-heating. We recall that the thermal inertia is defined as follows:

$$I = \sqrt{K\rho c_p}. \quad (3)$$

Part II, instead, is related to the estimation of the heat released in the subsurface of Oxia Planum by the drilling operations. We finally provide an estimation of the lifetime of the hypothetical ice-rich sphere in contact with the tip of the drill.

3.1. Influence of the Thermal Inertia. In the top panels of Figure 2, we report the temperature plot vs. time at different depths from the surface for models A, B, and C (respectively, from left to right). The temperatures are calculated along a line in the z-direction perpendicular to the surface passing through the center. In model A, the surface temperature oscillates between 175 K and 265 K, while in model B, it oscillates between 185 and 255 K, a result very similar to model A since thermal conductivities of these models are of the same order of magnitude. Conversely, in model C, the oscillations of the surface temperature are reduced because of the higher thermal conductivity and consequently the higher thermal inertia: in this case, the surface temperature is in the range 200–245 K.

In the bottom panels of Figure 2, we show the temperature vs. depth profile at different moments of the Martian day: we select the point of minimum temperature ($p1$) in the "day-night temperature profile," the inflexion point ($p2$) before the maximum ($p3$), and the inflexion point ($p4$) after the maximum. See Figure 3. These plots provide information about the skin depth, i.e., the depth at which the amplitude of the thermal wave is attenuated by a factor $1/e$. We recall that the diurnal skin depth is defined as

$$\delta = \frac{I}{\rho c_p}\sqrt{\frac{P}{\pi}}, \quad (4)$$

where P is the rotational period. Since the temperature profiles converge at about 30 cm in models A and B, we can deduce that this value represents the skin depth; in model C, instead, the skin depth is about 40 cm.

3.2. Influence of the Density. In this section, we would like to demonstrate that, fixed the thermal conductivity (and the specific heat), if we use different values for the density, the surface temperature does not change in a significant way as shown in Figure 4(a). As a test case, we adopt model C: we compare the surface temperature in case of density of 1900 $\mathrm{kgm^{-3}}$, 2700 $\mathrm{kgm^{-3}}$, and 3000 $\mathrm{kgm^{-3}}$. The value 1900 $\mathrm{kgm^{-3}}$ could correspond, for example, to hydrated vermiculite while 3000 $\mathrm{kgm^{-3}}$ to dehydrated nontronite or chlorite [23]. We observe no differences between the case with 2700 $\mathrm{kgm^{-3}}$ and 3000 $\mathrm{kgm^{-3}}$ and a slight difference with the case with 1900 $\mathrm{kgm^{-3}}$ in the maximum and minimum values reached: for instance, the maximum values differ of less than 5 K. We conclude that the density affects the surface temperatures only in a marginal way, unlike the thermal conductivity as previously shown since these parameters can change in a very significant way.

Table 1: Thermophysical parameters adopted in the first part of this work. Models A and B correspond to a thermal inertia of 160 TIU and 255 TIU, respectively. They are characterized by a composition similar to high-porous sedimentary rocks. Model C, instead, is characterized by a high thermal inertia (650 TIU), compatible with a composition clay dominant (e.g., vermiculite).

Parameter	Value	Reference
Distance	1.67 AU	This study
Initial temperature	200 K	This study
Specific heat	800 $\mathrm{J\,kg^{-1}K^{-1}}$	[20]
Albedo	0.13	[18]
Latitude	18°	[4]
Model A ($I = 160$ TIU)		
Density	1700 $\mathrm{kgm^{-3}}$	[21]
Thermal conductivity	0.018 $\mathrm{Wm^{-1}K^{-1}}$	[22]
Model B ($I = 225$ TIU)		
Density	1700 $\mathrm{kgm^{-3}}$	[21]
Thermal conductivity	0.048 $\mathrm{Wm^{-1}K^{-1}}$	[22]
Model C ($I = 650$ TIU)		
Density	2700 $\mathrm{kgm^{-3}}$	[23]
Thermal conductivity	0.2 $\mathrm{Wm^{-1}K^{-1}}$	This study

3.3. Influence of Self-Heating. In order to evaluate the contribution due to self-heating among the facets of the shape model under study, we carried out a further simulation using model A as the test case but without self-heating. In Figure 4(b), we show the result, plotting only the surface temperature: we observe that the peak difference is about 10 K. Self-heating is taken into account with the algorithm of the hemicube, implemented in the COMSOL Multiphysics code used for these simulations. In Figure 5, we report the 3D Martian surface temperature map for model A in order to point out how the temperature can increase where the surface roughness is high. Maps refer to one planetary rotation.

3.4. Heat Released by the Drilling. The second part of this work concerns the estimation of the heat released during the drilling operations. This contribution is important to evaluate the lifetime of possible volatile species in the subsurface of Mars. The geometry adopted in this second part of the work is shown in Figure 6.

To take into account this contribution in a simple way, we imposed a heat frictional flux on the sides, "in contact" with the drill (represented by the cylinder of Figure 6), of our domain of integration. This heat flux is defined by the following equation (e.g., [33, 34]):

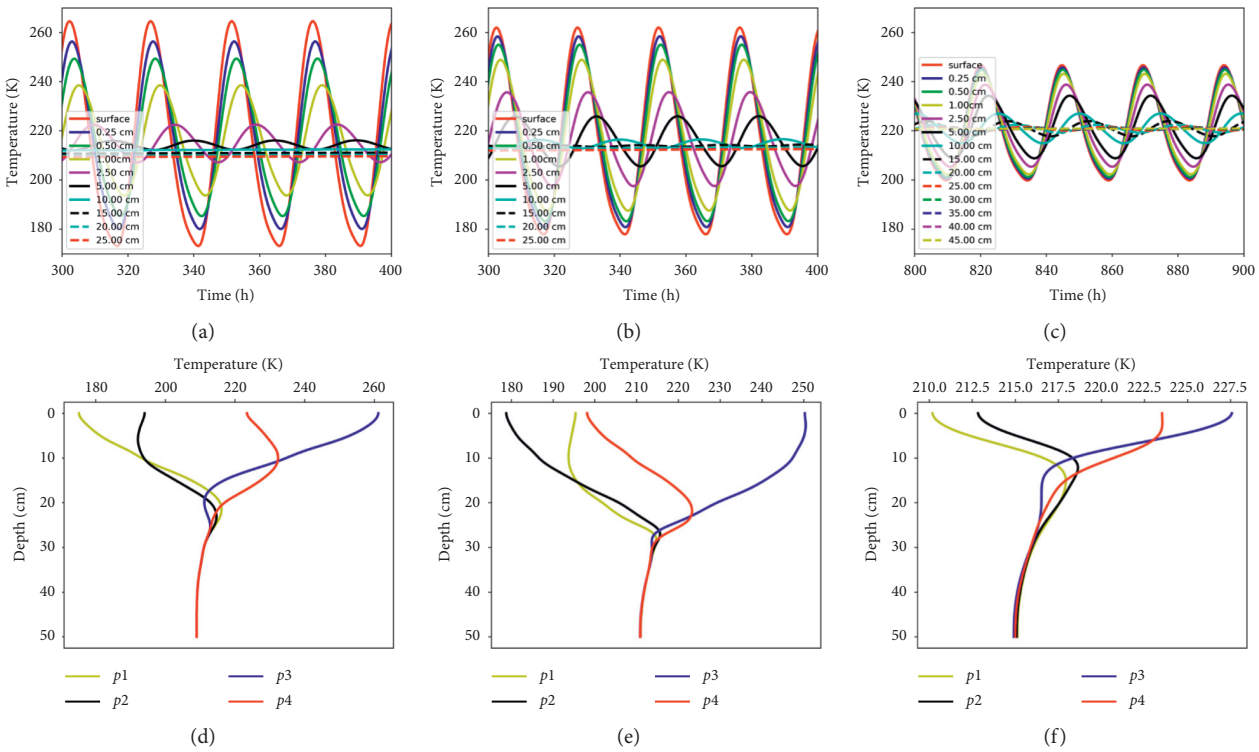

FIGURE 2: In panels (a–c), we show the temperature profiles versus time for the three models developed in this work. Different depths from the surface are explored. Note that, for model C, more depths are reported than models A and B since the skin depth is greater. The time reported on the x-axis is that required to reach the steady state, so we report only the last planetary rotations. In panels (d–f), we show the temperature profile vs. depth at the particular moment of the Martian day: $p1$ represents the minimum point in the "day-night" temperature plot, $p3$ the maximum point, and $p2$ and $p4$ the inflexion points before and after the maximum, respectively. Also, see Figure 3.

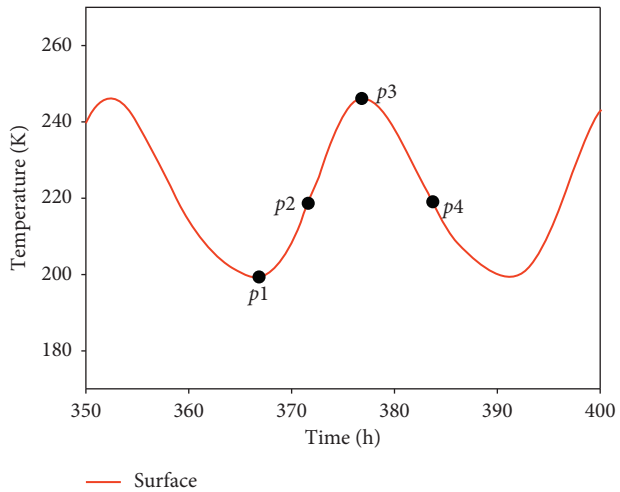

FIGURE 3: Points to which the profiles of temperature vs. depth in Figure 2 refer to. The points correspond to the minimum ($p1$), the inflexion point ($p2$) before the maximum ($p3$), and the inflexion point ($p4$) after the maximum. This day-night profile is merely indicative.

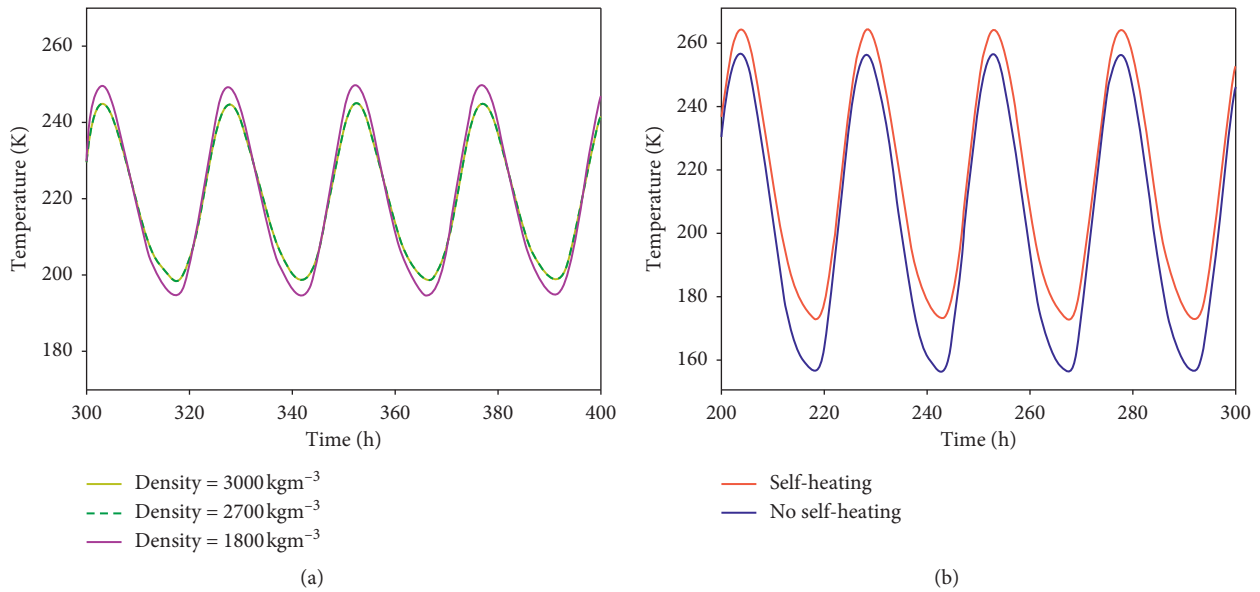

Figure 4: (a) Temperature dependence on density: we used model C as the test case. (b) Evaluation of self-heating contribution in case of model A used as the test case: red plot includes self-heating, while the blue plot does not.

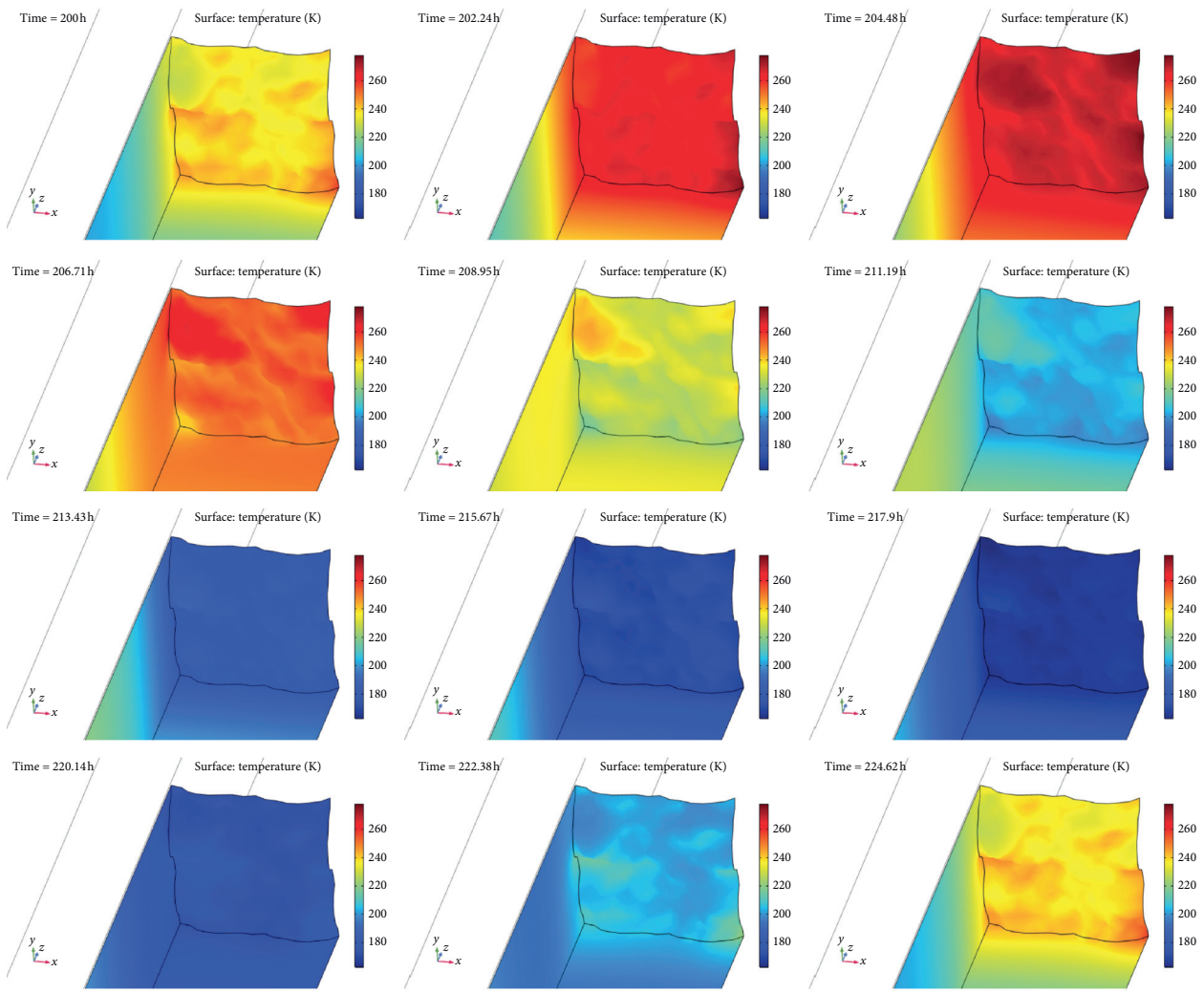

Figure 5: 3D temperature maps along a Martian day for model A. Maps refer to the Martian surface. The time on the top left is time elapsed from the beginning of simulation.

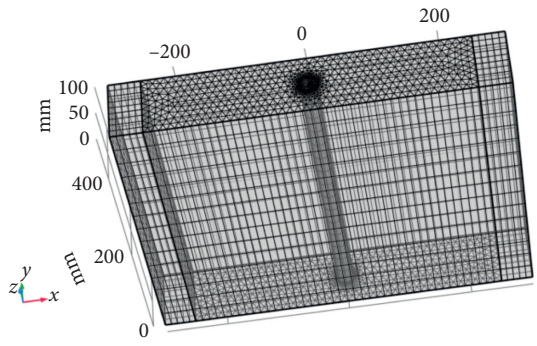

Figure 6: Geometry adopted in the second part of this work. A cylinder with a radius of 13 mm (the thickness of the drill tip [29]) simulated the hole of the drill. The depth is assumed to be equal to 50 cm, compatible with the length of a rod [29].

$$\Phi = \frac{\eta F_n \omega r}{\pi r h} \left[\mathrm{W m^{-2}}\right], \tag{5}$$

where η is the coefficient of friction, ω is the rotational velocity, r is the radius of the "hole," i.e., the thickness of the tip, and h is the height of the domain of integration (50 cm). The coefficients of friction explored are 0.3 and 0.9. Coefficient of friction represents a sort of heat transfer efficiency, from the drill to the soil. The value of 0.3 is compatible with the ones used in [35]: we also test a frictional heating coefficient close to the unit, i.e., 0.9. We select two values for the rotation for minutes (hereafter rpm): 30 and 60 [29]. The total integration time is 90 min, while the time step is 10 s. We simulate a "drilling window" as in Figure 7: we start with 30 min in "on mode," followed by 30 min in "off mode" and, finally, other 30 min in "on mode." Some assumptions are made:

(i) Instantaneous drilling (drill excavation is not modeled)

(ii) Constant thrust

(iii) Constant rotational velocity

For the domain of integration (i.e., the Martian subsurface), we used the values of model C, i.e., $K = 0.2\ \mathrm{W m^{-1} K^{-1}}$, $\rho = 2700\ \mathrm{kg m^{-3}}$, and $c_p = 800\ \mathrm{J kg^{-1} K^{-1}}$; however, also using the parameters of models A and B, the results are very close.

In Table 2, we report the thermophysical parameters adopted in the second part of this work.

In Figure 8, we report the 1D temperature profile along the y-direction at $x = 0$ and $z = 50$ cm (maximum depth; see Figure 6): in the x-axis, we report the distance from the hole. The shadowed red rectangle identifies the drill. At $z = 50$ cm, we want to point out that the solar input is negligible, so the initial temperature at that temperature, before the drilling, is reasonably close to the equilibrium temperature, i.e., 200 K. We selected four times (20, 43, 65, and 90 minutes). We observe that, in the case of $\mu = 0.3$ and rpm = 30, the maximum increase in temperature due to the drilling operations is about 55 K. The increase results in about 75 K if we use rpm = 60. If we adopt a frictional heating coefficient of 0.9, the increase in temperature is about 90 K for rpm = 30 and very high, more than 100 K, for rpm = 60.

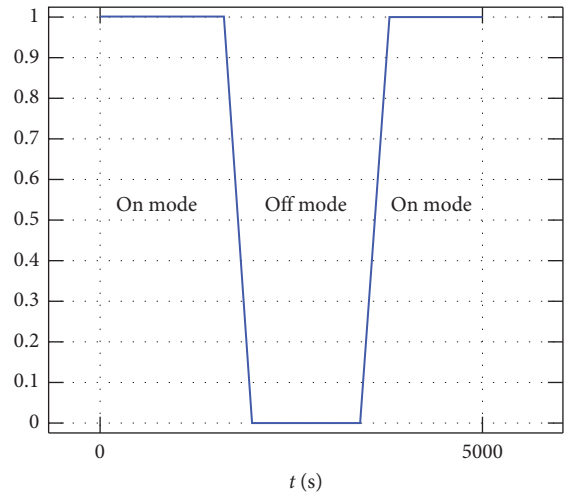

Figure 7: Drilling window adopted in this work: first 30 minutes in "on mode," followed by 30 minutes in "off mode" and, finally, other 30 minutes in "on mode." The values on the y-axis represent a sort of efficiency. The heat flux described in equation (5) is multiplied for this function: there is a gradual transition between on mode and off mode.

Table 2: Thermophysical parameters adopted in the second part of this work.

Parameter	Value	Reference
Thrust	300 (N)	[29]
rpm	30–60	[29]
Friction coefficient	0.3**–0.9	This study
Tip density	3500 ($\mathrm{kg m^{-3}}$)	[35]
Tip thermal conductivity	540 ($\mathrm{W m^{-1} K^{-1}}$)	[35]
Tip specific heat	790 ($\mathrm{J kg^{-1} K^{-1}}$)	[35]
Drill activity	90 (min)	This study

**Compatible with [35].

3.4.1. Lifetime of Subsurface Ices. At this point, we can calculate the rate of sublimation of hypothetical subsurface ices from one basis of the cylinder (i.e., the borehole). We applied the following formula [36]:

$$\Gamma = P_{\mathrm{sat}} \sqrt{\frac{\mu}{2\pi R T}}, \tag{6}$$

where Γ is expressed in $\mathrm{kg m^{-2} s^{-1}}$. R is the universal gas constant, while μ is the water molecular weight. The water ice saturation pressure is defined as in [37]:

$$P_{\mathrm{sat}} = \exp\left(9.550426 - \frac{5723.265}{T} + 3.53068 \ln T - 0.00728332 T\right), \tag{7}$$

valid for $T > 110$ K.

Equation (6) holds at the surface: in order to take into account the effects of crust thickness (h), we multiply Γ by (r_p/h), as in [38]. We set $r_p = 3$ mm as the expected grain

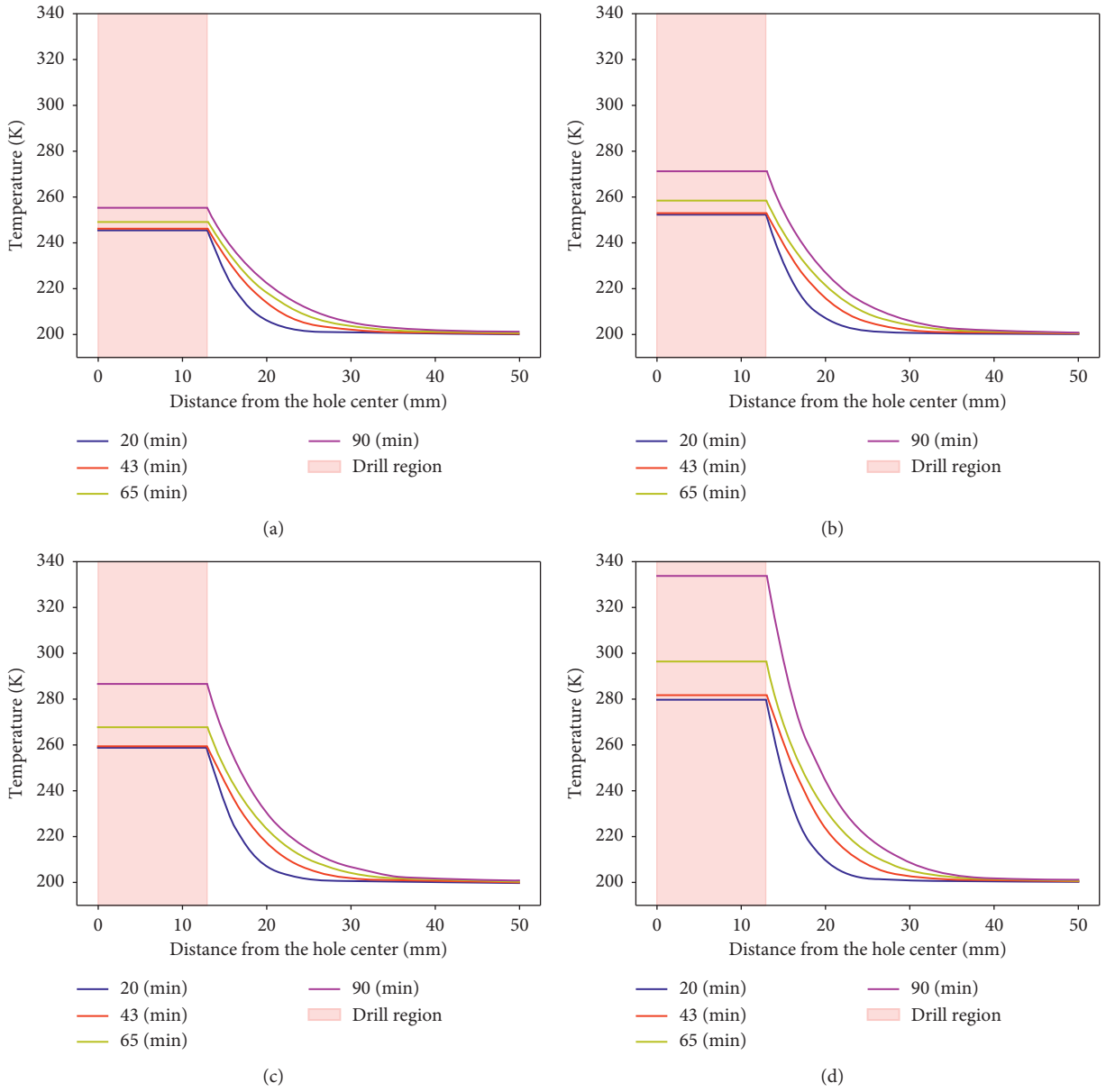

FIGURE 8: (a) $\mu = 0.3$ and rpm = 30; (b) $\mu = 0.3$ and rpm = 60; (c) $\mu = 0.9$ and rpm = 30; (d) $\mu = 0.9$ and rpm = 60. For the Martian subsurface, we used $K = 0.2\,\mathrm{W m^{-1} K^{-1}}$, $\rho = 2700\,\mathrm{kg m^{-3}}$, and $c_p = 800\,\mathrm{J kg^{-1} K^{-1}}$.

size at Oxia Planum [18]. In Figure 9, we observe that, in the "hottest case" ($\eta = 0.9$ and rpm = 60), the sublimation rate is tens of $\mathrm{kg\,m^{-2} s^{-1}}$, while in the "coldest case" ($\eta = 0.3$ and rpm = 30), the sublimation rate is about $0.2\,\mathrm{kg\,m^{-2} s^{-1}}$.

As in [39], we can calculate the lifetime of an ice deposit of mass m_0. For simplicity, we use a spherical form with initial radius equal to the radius of the drill tip. The variation of the radius as a function of the time is related to the sublimation rate by the following formula:

$$\frac{dr}{dt} = -\frac{\Gamma}{\rho_{\mathrm{ice}}}, \tag{8}$$

where for ρ_{ice}, we used $950\,\mathrm{kg\,m^{-3}}$. After integrating equation (8) and using the Taylor series around r_0, we obtain the relative loss of ice mass at time t after the deposit is raised to temperature T:

$$\frac{m(t)}{m_0} = \left[1 - \frac{\Gamma t}{\rho_{\mathrm{ice}} r_p}\right], \tag{9}$$

where t is the time expressed in seconds. By using the maximum sublimation rate (Γ), we obtain that, in case of $\eta = 0.3$ and rpm = 30, the fraction of initial mass remaining after 90 minutes is about 60 %, in case of $\eta = 0.3$ and

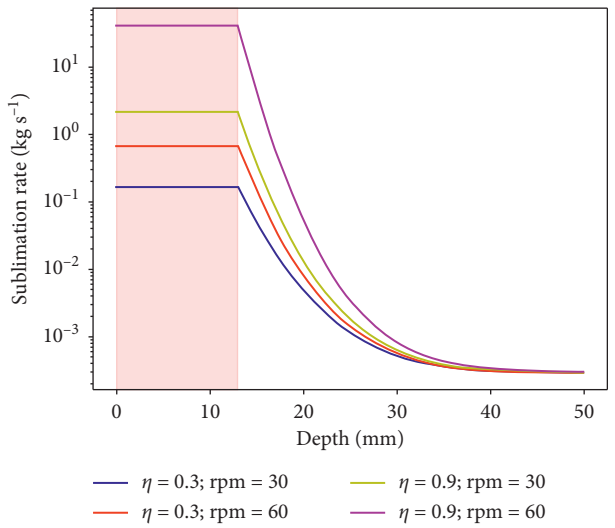

Figure 9: Sublimation rate for the explored cases of Figure 8. The rate of sublimation is calculated through one basis of the cylinder representing the borehole.

rpm = 60, it is about 1%, while in the other two cases (η = 0.9 and rpm = 30 or 60), we have a complete loss of the initial mass.

4. Discussion and Conclusions

In this work, we explored the dependence of the thermal inertia on the subsurface temperatures of Oxia Planum, the landing site of the mission ExoMars 2022, and we also evaluated the heat released by the drilling operations. In particular, in the first part, we investigated the influence of the thermal inertia on the subsurface temperatures by testing three models: model A, characterized by a thermal inertia of 160 TIU, compatible with $K = 0.018\ \mathrm{Wm^{-1}K^{-1}}$; model B characterized by a thermal inertia of 255 TIU, compatible with $K = 0.048\ \mathrm{Wm^{-1}K^{-1}}$; and model (C) characterized by a thermal inertia of 650 TIU, compatible with $K = 0.2\ \mathrm{Wm^{-1}K^{-1}}$. Models A and B are moreover characterized by a low density, i.e., 1700 $\mathrm{kgm^{-3}}$, compatible with a composition made of high-porous sedimentary rocks; model C, instead, is characterized by a density of 2700 $\mathrm{kgm^{-3}}$, compatible with a clay dominant composition (e.g., vermiculite). The heliocentric distance considered in these simulations is the aphelion since the landing is currently planned, while Mars is very close to the aphelion.

In model A, the surface temperature ranges from 175 K to 265 K, while in model B, it ranges from 175 K to 255 K. The behaviour is very similar since thermal conductivities of these models are of the same order of magnitude. In these cases, the skin depth is close to 30 cm. The situation is different for model C: here, in fact, the oscillations of the surface temperature are limited between 200 K and 245 K because of the high thermal inertia of this case (i.e., 650 TIU), and the skin depth is close to 40 cm. We also verified the effects of self-heating among the facets of the shape model by modeling the surface of our domain as a Gaussian random surface. The difference between the case with self-heating and without self-heating is about 10 K: we used model A as a test case.

The second part of the paper is dedicated to test the effect of the drilling activities on the subsurface thermal environment. We used different parameters to simulate the drilling characteristics as well as the subsurface conditions, including the presence of ice patches.

Heat released by the drilling operations has been simulated in different cases of friction: in the case of low frictional coefficient ($\eta = 0.3$), the maximum temperature increase at a depth of 50 cm is about 55 K (with rpm = 30) and about 75 K (with rpm = 60) after 90 minutes. In the case of high frictional heating ($\eta = 0.9$), the maximum temperature increase becomes 90 K (with rpm = 30) and 130 K (with rpm = 60). We also evaluated the behaviour of a hypothetical area with water ice in the subsurface: we calculated the sublimation rate and the lifetime of a hypothetical spherical ice-rich deposit, with a radius of 13 mm (the radius of the drill tip), using the temperature profiles obtained by the simulation of the drilling activity. After 90 minutes, the remaining ice mass is about 60% in case of η = 03 and rpm = 30, while in the other simulated cases, the remaining mass is negligible. However, a more complete treatment of the diffusion of possible volatiles in the subsurface of Mars will be addressed in the next paper.

The simulations reported here suggest that the thermal environment of the Martian subsurface can be strongly influenced by the drilling activity, with consequent changes in the characteristics of the subsurface areas and layers in the immediate vicinity of the borehole and in contact with the drill tip and rods. These thermal changes, induced by the heat released by the drilling, can contribute to variations in the original volatile content of the subsurface layers, including the possible loss of water ice, if initially present.

The results obtained by our numerical simulations offer a first depiction of thermal state, after the drilling, of the subsurface of Oxia Planum, because some assumptions were made in this work, in particular, we considered the drilling as an instantaneous process without treating excavation. Moreover, we applied the flux defined by equation (5) in an equal way to all the walls representing the contact sides with the drill. However, in order to increase the possibility of survival of any volatiles inside the subsurface of Oxia, we would reduce frictional heating or adopting appropriate window drilling. Future improvements will be made as well as a validation with laboratory experiments.

Data Availability

The data used to support this study are included at https://github.com/MiFormisano/Oxia_Planum.

Conflicts of Interest

The authors declare that they have no conflicts of interest.

Authors' Contributions

All authors either contributed directly to the researcher viewed and/or assisted in the analysis, writing, editing, and/ in searching for and referencing the works cited.

Acknowledgments

This work was funded by the Italian Space Agency (ASI) (ASI-INAF n. 2017-412-H.0).

References

[1] F. Da Pieve, G. Gronoff, J. Guo, and C. Mertens, "Radiation environment and doses on Mars at Oxia Planum and Mawrth Vallis: support for exploration at sites with high biosignature preservation potential," *Journal of Geophysical Research: Planets*, vol. 126, no. 1, Article ID e06488, 2021.

[2] D. Domagal-Goldman Shawn, K. E. Wright, K. Adamala et al., "The astrobiology primer v2.0," *Astrobiology*, vol. 16, no. 8, pp. 561–653, 2016.

[3] J. L. Vago, F. Westall, A. J. Coates et al., "Habitability on early Mars and the search for biosignatures with the ExoMars rover," *Astrobiology*, vol. 17, no. 6-7, pp. 471–510, 2017.

[4] C. Quantin-Nataf, J. Carter, L. Mandon et al., "Oxia planum: the landing site for the exomars rosalind franklin rover mission: geological context and prelanding interpretation," *Astrobiology*, vol. 21, no. 3, Article ID 33400892, 2021.

[5] J. Carter, C. Quantin, P. Thollot, D. Loizeau, A. Ody, and L. Lozach, "Oxia planum: a clay-laden landing site proposed for the exomars rover mission: aqueous mineralogy and alteration scenarios," in *Proceedings of the 47th Lunar and Planetary Science Conference*, p. 2064, The Woodlands, TX, USA, March 2016.

[6] L. Mondon, "Morphological and spectral diversity of the clay-bering unit at the ExoMars landing site Oxia planum," *Astrobiology*, vol. 21, pp. 464–480, 2021.

[7] A. Kereszturi, B. Bradak, E. Chatzitheodoridis, and G. Ujvari, "Indicators and methods to understand past environments from ExoMars rover drills," *Origins of Life and Evolution of Biospheres*, vol. 46, no. 4, pp. 435–454, 2016.

[8] A. Coradini, G. Piccioni, S. Amici et al., "MA_MISS: Mars multispectral imager for subsurface studies," *Advances in Space Research*, vol. 28, no. 8, pp. 1203–1208, 2001.

[9] S. De Angelis, M. C. De Sanctis, E. Ammannito, C. Carli, T. Di Iorio, and F. Altieri, "The MA_Miss instrument performance, I: analysis of rocks powders by Martian VNIR spectrometer," *Planetary and Space Science*, vol. 101, pp. 89–107, 2014.

[10] M. C. De Sanctis, F. Altieri, E. Ammannito et al., "Ma MISS on ExoMars: mineralogical characterization of the martian subsurface," *Astrobiology*, vol. 17, no. 6-7, pp. 612–620, 2017.

[11] S. De Angelis, M. C. De Sanctis, E. Ammannito, C. Carli, T. Di Iorio, and F. Altieri, "The Ma_Miss instrument performance, II: band parameters of rocks powders spectra by Martian VNIR spectrometer," *Planetary and Space Science*, vol. 117, pp. 329–344, 2015.

[12] J. Jean-Luc, F. Westall, B. A. Hofmann et al., "The close-up imager onboard the esa exomars rover: objectives, description, operations, and science validation activities," *Astrobiology*, vol. 17, no. 6-7, pp. 595–611, Article ID 28731819, 2017.

[13] A. Malakhov, I. Mitrofanov, M. Litvak et al., "Local water-rich areas on Mars found by the FREND neutron telescope onboard ExoMars TGO," in *Proceedings of the 14th European Planetary Science Congress (EPSC2020)*, p. 961, Helsinki, Finland, September 2020.

[14] Y. He, A. Buch, C. Szopa et al., "Influence of calcium perchlorate on the search for organics on Mars with tetramethylammonium hydroxide thermochemolysis," *Astrobiology*, vol. 21, no. 3, 2021.

[15] T. G. Wasilewski, "Evaluation of drilling-based water extraction methods for Martian ISRU from mid-latitude ice resources," *Planetary and Space Science*, vol. 158, pp. 16–24, 2018.

[16] K. Zacny and G. Cooper, "Considerations, constraints and strategies for drilling on Mars," *Planetary and Space Science*, vol. 54, no. 4, pp. 345–356, 2006.

[17] N. Putzig, M. Mellon, K. Kretke, and R. Arvidson, "Global thermal inertia and surface properties of Mars from the MGS mapping mission," *Icarus*, vol. 173, no. 2, pp. 325–341, 2005.

[18] E. Jones, G. Caprarelli, F. Mills, B. Doran, and J. Clarke, "An alternative approach to mapping thermophysical units from martian thermal inertia and albedo data using a combination of unsupervised classification techniques," *Remote Sensing*, vol. 6, no. 6, pp. 5184–5237, 2014.

[19] C. E. Gary-Bicas and A. D. Rogers, "Geologic and thermal characterization of Oxia planum using Mars odyssey THEMIS data," *Journal of Geophysical Research: Planets*, vol. 126, no. 2, Article ID e2020JE006678, 2021.

[20] M. Formisano, C. Federico, S. De Angelis, M. C. De Sanctis, and G. Magni, "A core dynamo in Vesta?" *Monthly Notices of the Royal Astronomical Society*, vol. 458, no. 1, pp. 695–707, 2016.

[21] K. W. Lewis, S. Peters, K. Gonter et al., "A surface gravity traverse on Mars indicates low bedrock density at Gale crater," *Science*, vol. 363, no. 6426, pp. 535–537, 2019.

[22] T. Spohn, M. Grott, S. E. Smrekar et al., "The heat flow and physical properties package (HP3) for the InSight mission," *Space Science Reviews*, vol. 214, no. 5, p. 96, 2018.

[23] V. I. Osipov, "Density of clay minerals," *Soil Mechanics and Foundation Engineering*, vol. 48, no. 6, pp. 231–240, 2012.

[24] M. Formisano, C. Federico, M. C. De Sanctis et al., "Thermal stability of water ice in ceres' craters: the case of juling crater," *Journal of Geophysical Research: Planets*, vol. 123, no. 9, pp. 2445–2463, 2018.

[25] M. Formisano, M. C. De Sanctis, S. De Angelis, J. D. Carpenter, and E. Sefton-Nash, "Prospecting the Moon: numerical simulations of temperature and sublimation rate of a cylindric sample," *Planetary and Space Science*, vol. 169, pp. 8–14, 2019.

[26] M. Formisano, C. Federico, G. Magni, A. Raponi, M. C. De Sanctis, and A. Frigeri, "Surface temperatures and water ice sublimation rate of oxo crater: a comparison with juling crater," *Journal of Geophysical Research (Planets)*, vol. 124, no. 1, pp. 2–13, 2019.

[27] A. Longobardo, V. Della Corte, A. Rotundi et al., "67P/Churyumov-Gerasimenko's dust activity from pre- to post-perihelion as detected by Rosetta/GIADA," *Monthly Notices of the Royal Astronomical Society*, vol. 496, no. 1, pp. 125–137, 2020.

[28] G. Rinaldi, M. Formisano, D. Kappel et al., "Analysis of night-side dust activity on comet 67P observed by VIRTIS-M: a new method to constrain the thermal inertia on the surface," *Astronomy & Astrophysics*, vol. 630, p. A21, 2019.

[29] E. Re, P. Magnani, M. Izzo et al., "Exomars multi rod drill development and testing," 2008.
[30] H. U. Keller, S. Mottola, B. Davidsson et al., "Insolation, erosion, and morphology of comet 67P/Churyumov-Gerasimenko," *Astronomy & Astrophysics*, vol. 583, p. A34, 2015.
[31] X. Shi, X. Hu, H. Sierks et al., "Sunset jets observed on comet 67P/Churyumov-Gerasimenko sustained by subsurface thermal lag," *Astronomy & Astrophysics*, vol. 586, p. A7, 2016.
[32] N. I. Komle, W. Macher, P. Tiefenbacher, and G. Kargl, "Three-dimensional illumination and thermal model of the Abydos region on comet 67P/Churyumov-Gerasimenko," *Monthly Notices of the Royal Astronomical Society*, vol. 469, no. 2, pp. S2–S19, 2017.
[33] A. T. Kuzu, K. R. Berenji, B. C. Ekim, and M. Bakkal, "The thermal modeling of deep-hole drilling process under MQL condition," *Journal of Manufacturing Processes*, vol. 29, pp. 194–203, 2017.
[34] S. F. Miller, R. Li, H. Wang, and A. Shih, "Experimental and numerical analysis of the friction drilling process," *Journal of Manufacturing Science and Engineering-ASME*, vol. 128, no. 3, 2006.
[35] M. Yahiaoui, L. Gerbaud, J.-Y. Paris, J. Denape, and A. Dourfaye, "A study on PDC drill bits quality," *Wear*, vol. 298, pp. 32–41, 2013.
[36] A. H. Delsemme and D. C. Miller, "Physico-chemical phenomena in comets—III: the continuum of comet Burnham (1960 II)," *Planetary and Space Science*, vol. 19, no. 10, pp. 1229–1257, 1971.
[37] D. M. Murphy and T. Koop, "Review of the vapour pressures of ice and supercooled water for atmospheric applications," *Quarterly Journal of the Royal Meteorological Society*, vol. 131, no. 608, pp. 1539–1565, 2005.
[38] M. E. Landis, S. Byrne, N. Schörghofer et al., "Conditions for sublimating water ice to supply ceres' exosphere," *Journal of Geophysical Research: Planets*, vol. 122, no. 10, pp. 1984–1995, 2017.
[39] E. L. Andreas, "New estimates for the sublimation rate for ice on the Moon," *Icarus*, vol. 186, no. 1, p. 2430, 2007.

Hindawi
Advances in Astronomy
Volume 2021, Article ID 5516892, 12 pages
https://doi.org/10.1155/2021/5516892

Review Article

Small Mars Mission Architecture Study

Claire E. Parfitt,[1] **Adam G. McSweeney**,[1] **Lisa De Backer**,[1] **Csilla Orgel**,[1] **Andrew J. Ball**,[1] **Michael Khan**,[2] **and Sanjay Vijendran**[1]

[1]*European Space Agency ESTEC, 2200 AG Noordwijk, Netherlands*
[2]*European Space Agency ESOC, Robert-Bosch-Strasse 5, Darmstadt, Germany*

Correspondence should be addressed to Claire E. Parfitt; claire.parfitt@esa.int

Received 29 January 2021; Accepted 21 May 2021; Published 10 June 2021

Academic Editor: Michael Kueppers

While the vast majority of ESA's funding for Mars exploration in the 2020s is planned to be invested in ExoMars and Mars Sample Return, there is an interest to assess the possibility of implementing a small mission to Mars in parallel with, or soon after, the completion of the MSR programme. A study was undertaken in the Concurrent Design Facility at ESA ESTEC to assess low-cost mission architectures for small satellite missions to Mars. Given strict programmatic constraints, the focus of the study was on a low-cost (<250MEuro Cost at Completion), short mission development schedule with a cost-driven spacecraft design and mission architecture. The study concluded that small, low-cost Mars missions are technically feasible for launch within the decade.

1. Introduction

ESA's current Mars exploration programme consists of the flying orbiters Mars Express and the ExoMars TGO, while the ExoMars rover *Rosalind Franklin* is planned for launch in 2022. The Nov 2019 ESA Council of Ministers meeting, Space19+, approved ESA contributions to a Mars Sample Return programme, led by NASA, with a launch of the sample retrieval missions planned to occur as early as 2026. ESA's primary MSR contributions include the Earth Return Orbiter as a dedicated mission, and the Sample Fetch Rover and Sample Transfer Arm of the NASA-led Sample Return Lander mission.

While the vast majority of ESA's funding for Mars exploration in the 2020s is planned to be invested in ExoMars and Mars Sample Return, there is an interest to assess, at Phase 0-level, the possibility of implementing a small mission to Mars in parallel with, or soon after, the completion of the MSR programme, to further the exploration of Mars in areas not addressed by MSR.

Missions to Mars at the small scale have not been greatly studied within ESA since Mars Express two decades ago and preliminary concepts for a Mars Micro Mission as an "Arrow" mission of the Aurora programme [1]. Since then, the landscape of technologies (in particular those relevant for small Low Earth Orbit platforms and instrumentation) and launch capabilities (e.g., rideshares) have matured significantly, offering promising new opportunities for low-cost implementations of interplanetary missions. The ESA programmatic framework with the advent of the Aurora programme, now European Exploration Envelope Programme (E3P), and approach to low-cost planetary missions has thus evolved over the years [2–5].

A study was undertaken in the Concurrent Design Facility at ESA ESTEC to assess low-cost mission architectures for small satellite missions to Mars. Given strict programmatic constraints, the focus of the study was on a low cost, short mission development schedule and with a cost-driven spacecraft design and mission architecture.

This paper presents an overview of the mission architectures considered and the results of mission and system-level design trades used to select a reference scenario for each mission case.

The final report of the CDF study [6] provides further details of all the subsystem design and performance analyses carried out by the team.

2. Mission Architecture

2.1. Approach to Mission Architecture Assessment. Due to the unique opportunity from which this study originates, the initial driving constraints were largely programmatic (rather than scientific or technical) and do not impose any particular kind of mission architecture. With a launch timed to complement the upcoming Mars Sample Return missions at the end of the 2020s, applying these constraints would mean having an opportunity for a European mission to Mars that provides *in situ* science data return to the Mars science community at a time when currently no new *in situ* science data are expected, as well as serving exploration goals towards the preparation of human Mars exploration.

Given the large trade space of potential options that could be considered for such a mission, a strategy with which to approach the mission architecture definition was devised. Initially, an assessment of the programmatic and cost constraints was developed into a set of high-level mission requirements and the design drivers formulated. A consultation with ESA Martian science experts revealed some mission themes that were turned into three distinct mission cases. These mission cases are representative of three different types of missions and are general enough to cover a wide variety of scenarios that scientists might like to see in a small Mars mission.

The architectural trade space was then analysed for key components of the mission architecture, such as launch scenario and the means of transfer to Mars. Various trade-offs were conducted at mission level to condense the options into a set of reference mission scenarios; one for each mission case.

2.2. Programmatic Constraints and Design Drivers. The following programmatic constraints were used to further limit the scope of study:

(i) The mission should be designed to cost

(ii) The project should envisage a fast development time, where a project phase of 4-5 years is considered

(iii) The time of transfer to final Mars orbit should be constrained to 3 (Earth) years

(iv) To limit the need for extensive developments, only equipment and units that can reach TRL 7/8 by PDR will be considered

The above constraints indicate that this mission is heavily cost and schedule driven. The study therefore aimed to address what can be achieved for a certain cost when there are no initial performance requirements placed on the resulting space segment. Whilst these design drivers remain the priority for ensuring a low-cost, short development time mission, it is still important that there is useful and attractive science return available from the mission. With this in mind, the science team helped to guide the evolution of the spacecraft design, ensuring that valuable science could be produced within the mass, power, and data envelopes under consideration and suggesting representative target orbits at Mars that would enable such missions, as well as reasonable targets for minimum payload allocations.

2.3. Selection of Mission Cases. Mission cases were selected to represent a broad range of missions that are of current interest to the ESA Mars Exploration Programme. Three representative mission cases were selected for study and are illustrated in Figure 1:

(1) *Mars Communications Constellation*. A three satellite constellation with an objective to provide data relay with continuous coverage to ground assets. The satellites also contain secondary science instrumentation.

(2) *Mars Science Orbiter*. A single science orbiter with a primary science objective and a secondary objective to provide a data relay.

(3) *Mars Hard Lander*. A demonstration mission of a carrier module and a number of hard landers.

2.4. Architecture Options. The study assessed a wide range of mission architectures. Given the wide scope of architectures that would be available for a cost-driven mission to Mars and the various mission cases under study, there are many potential options for the launch and transfer scenario. In order to condense these options, an initial qualitative assessment was made of launch vehicles, initial orbit injection options, and propulsions technologies that are likely to be available in the given timeframe.

The initial orbit into which the spacecraft is injected dictates the ΔV requirements needed for transfer to Mars. Options put forward for trade-off were LEO, GTO, the Earth-Sun L2 point, and direct trans-Mars Injection (TMI). The launch vehicles and corresponding injection orbits depicted in Figure 2 were considered. Whilst other similar options may become available opportunistically, the launch scenarios given here may be considered as representative for alternative launch vehicles of similar cost and performance.

In the case that direct trans-Mars Injection cannot be provided by the launch vehicle (e.g., due to insufficient performance or in case of a rideshare scenario), the spacecraft requires the capability to transfer to Mars from an initial geocentric orbit of its own accord. There are fundamentally three options available. The propulsion architecture options put forward for trade-off are shown in Figure 3.

Commercial rideshare options to GTO from which the satellite(s) would transfer to Mars using either chemical or electric propulsion were evaluated alongside dual and dedicated launch scenarios. The notable launch and transfer scenarios considered are depicted in Figure 4.

SEP-based transfers departing from LEO were not assessed as these were initially considered to take too long to achieve Earth escape conditions and impose significant radiation exposure on the spacecraft through extended dwelling in Earth's Van Allen Belts. Similarly CP-based transfers to LMO were assumed to necessitate aerobraking to limit overall mission ΔV requirements.

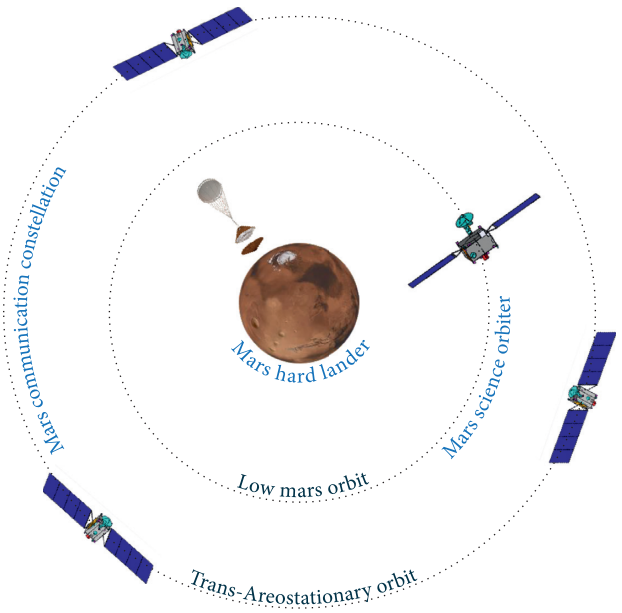

Figure 1: An overview of the three different mission cases studied in the CDF (not to scale).

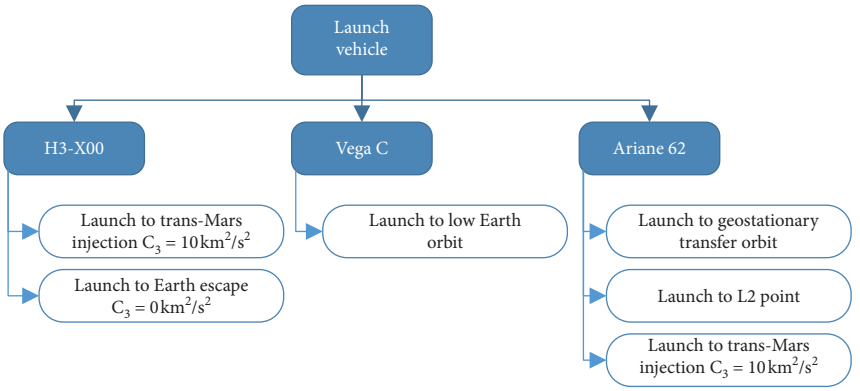

Figure 2: An overview of the launch vehicle options and corresponding injection orbits considered for study.

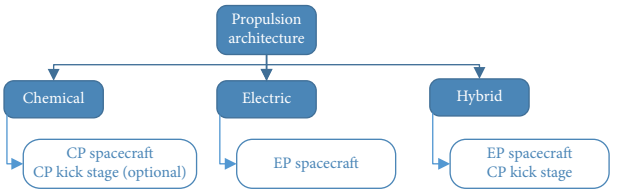

Figure 3: An overview of the propulsion architecture options considered for study.

Hybrid concepts were initially considered; however, these were later excluded, as the overall costs for the development of both a chemical kick-stage and a dedicated electric propulsion system were considered prohibitively high for the mission scenario.

An initial trade-off was made for each of the remaining combinations of launch and transfer options based on cost, performance, availability, operational complexity, and transfer time to Mars. From these results a reference architecture was selected for each mission case. The ΔV

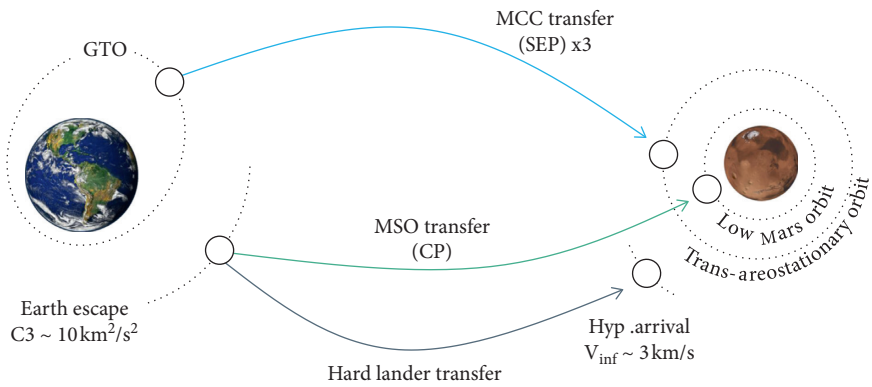

Figure 4: Overview of the propulsion architecture options considered for study. Solar electric propulsion (SEP) and chemical propulsion (CP) transfers are considered to reach low Mars orbit (LMO) and specific areosynchronous (AEO) orbits such as Trans-Areostationary (TASO).

combinations considered for both the Chemical Propulsion (CP) transfer cases and the Solar Electric Propulsion (SEP) transfer cases are provided in Tables 1 and 2.

3. Mars Communications Constellation Mission

Despite the long range, high altitude orbits are considered to be particularly useful for providing data relay to surface and orbiter missions due to their ability to provide long access times. This is complementary to the short range, short duration passes afforded by orbiters at low altitude. Areosynchronous orbits may be especially useful for this purpose since they have an orbit period similar to a Martian sol and are therefore a good candidate for the provision of continuous coverage of assets. Notably, such class of orbits can provide continuous coverage with far fewer spacecraft than would be required for a low Mars orbit (LMO) constellation.

Satellites in an areostationary orbit are subject to natural perturbations, which will incur added station keeping costs to maintain the spacecraft within prescribed mission required boundaries. There exist four regions of longitudinal stability for areostationary satellites, which require minimal station keeping costs [7]. However, these locations are evenly distributed and continuous coverage from these points can only be ensured by a constellation of minimum four spacecraft.

Following an initial trade-off on orbit design, a Trans-Areostationary Orbit (TASO) was selected for the Mars Communication Constellation (MCC) mission. This type of orbit has a slightly greater semimajor axis than areostationary orbits and allows the constellation to drift slowly around Mars, maintaining continuous coverage of the surface with minimal station keeping costs. Uninterrupted coverage is provided up to latitudes of $\pm 70^{\circ}$ for an elevation angle of 10°, as shown in Figure 5.

A Trans-Areostationary Orbit enables near-global simultaneous and continuous full-disk observation up to high latitudes (excluding the polar regions) of Mars. The view from the three satellites allows the monitoring of dynamical phenomena rapidly evolving in space and time. Various science and exploration knowledge gaps could be addressed from the vantage points such as the exchange between the surface and the atmosphere (e.g., energy and mass balance), atmospheric phenomena (e.g., dust storms, water, and CO_2 clouds), interaction of solar wind with Mars's upper atmosphere, and the Martian moons [8]. Figure 6 shows the science activities enabled at different orbit configurations, target distance, and a range of angular resolutions of any imaging instrument.

The primary payload of the Mars Communications Constellation mission is the telecommunications package; however, an allocation is also made for a secondary science payload suite.

To select the science objectives, European and US priorities as stated in the MEPAG Science Objectives [10] were considered, with the aim of closing as many knowledge gaps as possible. Additionally, there is an aim to fit the science objectives to instruments that would be useful from a 17,600 km altitude TASO orbit, i.e., without the need for fine spatial resolution, considering payloads having high TRL and low mass and benefitting from the near-global (excluding the polar regions) simultaneous and continuous view from the three satellites, and observations throughout the full diurnal cycle.

The rapidly evolving dynamics of meteorological phenomena such as dust storms (timescale spans from a few hours to months) and water/CO_2 ice clouds (timescale spans from half an hour or less) could extend from mesoscale up to the planetary scale. They affect the energy balance and the distribution of aerosols in the atmosphere and support an argument for continuous and simultaneous observations across the planet [8].

The solar radiation energy balance at the surface depends on local topography, albedo, and spatial and temporal variations of atmospheric aerosols, which results in rapid changes of the lower atmospheric column. The mechanism of dust lifting, vertical mixing, transportation, and sedimentation are dependent on the diurnal variability [11]. Transportation of dust can reach the mid atmosphere within hours [12] and can significantly grow by a factor of 10-20 in area in a week or two ([13–16]). Water and CO_2 ice clouds form in topographic lows such as canyons and large impact

Table 1: Overview of the approximate transfer ΔV (m/s) assumed for different mission options for chemical propulsion (CP) concepts.

		Transfer to			
Transfer from	Hyperbolic arrival orbit	4-Sol orbit	TASO	LMO	LMO (with aerobraking)
4-Sol orbit	n/a	n/a	640 m/s	1,380 m/s	270 m/s
MTO/TMI	n/a	1,100 m/s	1,740 m/s	2,480 m/s	1,370 m/s
GTO	1,980 m/s	3,080 m/s	3,720 m/s	4,460 m/s	3,350 m/s
LEO	3,970 m/s	5,070 m/s	5,710 m/s	6,450 m/s	5,340 m/s

Table 2: Overview of the approximate transfer ΔV (m/s) assumed for different mission options for solar electric propulsion (SEP) concepts.

		Transfer to		
Transfer from	Earth escape C_3~0 km^2/s^2	Mars arrival V_∞~0 km/s	TASO	LMO
Mars arrival V_∞~0 km/s	n/a	n/a	1,000 m/s	3,000 m/s
Earth escape C_3~4 km^2/s^2	n/a	4,000 m/s	5,000 m/s	7,000 m/s
Earth escape C_3~0 km^2/s^2	n/a	5,700 m/s	6,700 m/s	8,700 m/s
GTO	3,700 m/s	9,400 m/s	10,400 m/s	12,400 m/s

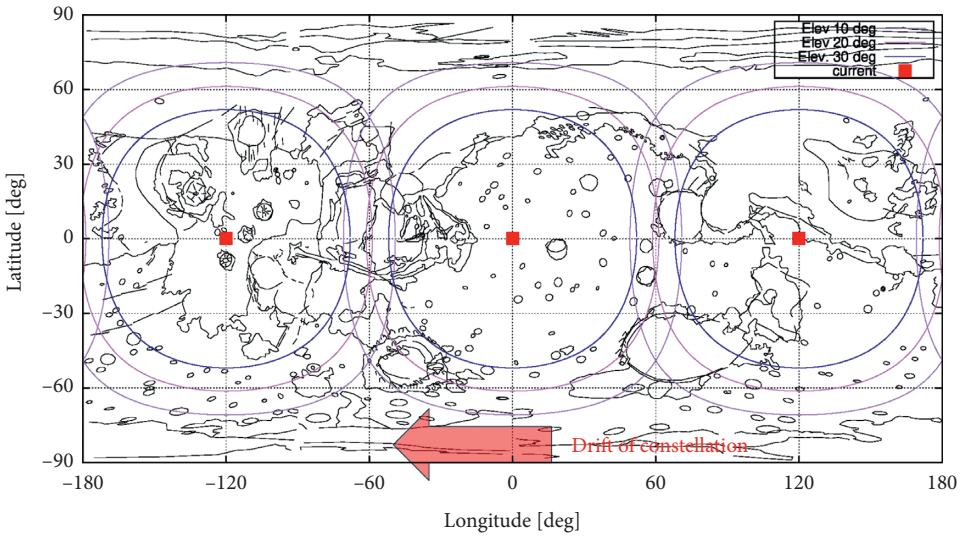

Figure 5: A Trans-Areostationary Orbit three-satellite constellation has Mars coverage up to latitudes of ±70°.

basins during the night and dissolve in the morning, implying an important exchange between the atmosphere and the regolith [17]. Additionally, cloud-tracking can provide information about the dynamic nature of dust storms and clouds.

The main science goal of the mission is to understand the present-day climate and dynamics of atmospheric processes. The following science objectives were considered:

(i) OBJ-01: characterize the volatiles (e.g., water and CO_2 clouds) and dust exchange (e.g., dust storms) between the surface and atmospheric reservoirs

(ii) OBJ-02: determine the spatial and temporal variation of key atmospheric gases

(iii) OBJ-03: measure the energy balance of the atmosphere

The science objectives (A2/1; A3/1, 2; A4/1, 3) from MEPAG Goal II (Atmospheric Science) [10] can be at least partially addressed by the proposed MCC mission.

Trade-offs were also made on the configuration of the spacecraft constellation during transfer, including consideration of three independent spacecrafts, a mother/daughter craft configuration, and the use of a disposable kick stage. Chemical, electric, and hybrid propulsion scenarios were all considered.

The resulting reference launch and transfer scenario for this mission is to utilise an Ariane 62 rideshare to a geostationary transfer orbit (GTO) and each of the three satellites will transfer to Mars independently, by means of onboard electric propulsion. This scenario, along with approximated ΔV needs, is illustrated in Figure 7.

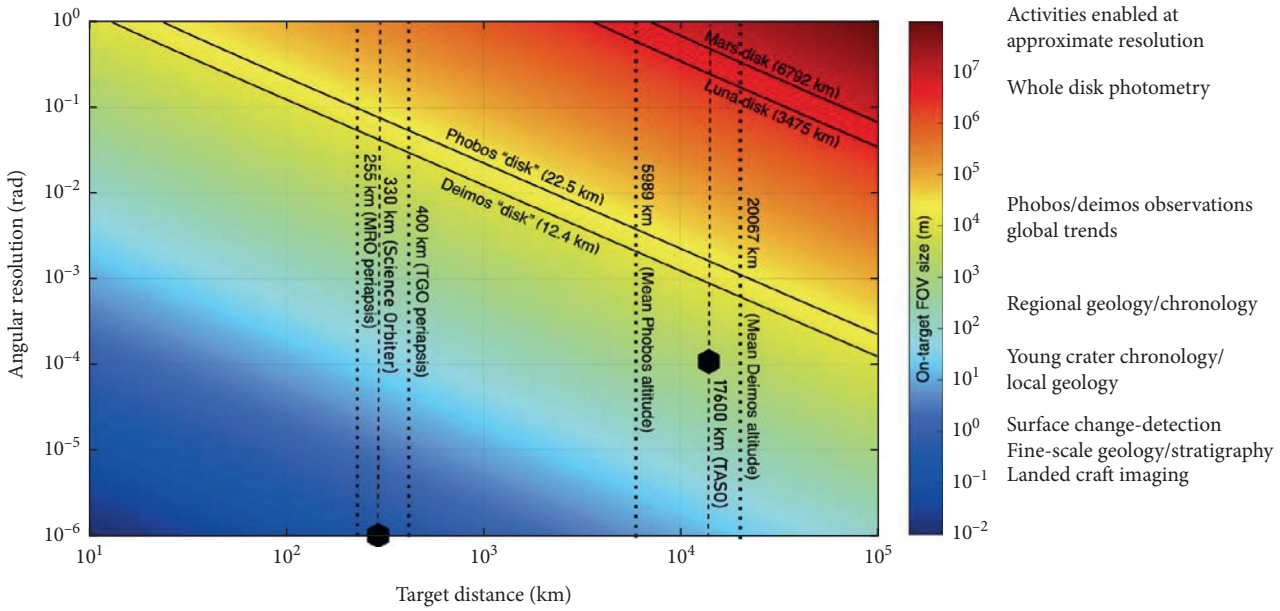

Figure 6: The science activities enabled at different orbit configurations; target distance is plotted against the angular resolution (=imaging capability of a camera). TASO at 17600 km altitude with current system requirements (10^{-4} angular resolution of the optical instrument, marked with black hexagon) enables full-disk monitoring and observation of regional processes (e.g., dust storms and clouds). The Science Orbiter (see Section 4) at 320 km altitude with current system requirements (10^{-6} angular resolution of the optical instrument, marked with black hexagon) supports high-resolution imaging of the surface (e.g., fine-scale geology, mineralogy, resources, and high-resolution topography), figure modified from [9].

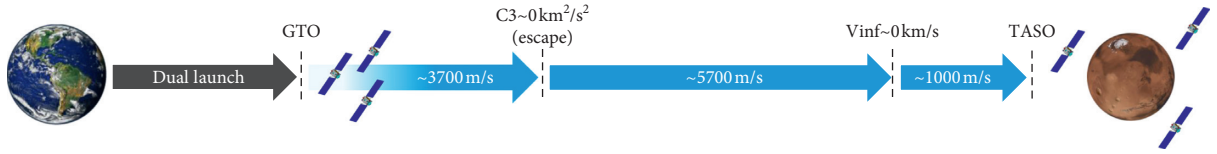

Figure 7: Launch and transfer scenario for the Mars Communication Constellation mission.

The end-state architecture of the constellation, including the communications concept, is illustrated in Figure 8. The satellite constellation must support communications with the current surface assets (rovers, probes, etc.) and therefore the Ultra High Frequency (UHF) band is selected as the communications link between the constellation and surface assets. Upgrades to S-band or X-band, to be in line with potential future mission needs, are to be investigated in the next design phases.

The instruments and their associated science objectives are given in Table 3.

The three satellites in the constellation are identical. A preliminary design exercise shows that a wet mass of ~610 kg per satellite is feasible within the programmatic constraints. This allows for a total launch mass that is consistent with an Ariane 62 dual launch opportunity to GTO and has a transfer time to Mars of 2.13 years. Mass reductions could be envisaged if the requirement to have a technology readiness level of 7/8 by PDR is relaxed or if a later launch opportunity is used.

The mass constraints placed by a dual launch opportunity in conjunction with the programmatic constraints mean that the performance of the telecommunications package is relatively low given the long range of the TASO orbit. This performance could be optimized, but it is important to note that even a low data rate link with continuous coverage fills an existing data gap. Mass budget information is provided in Table 4.

4. Mars Science Orbiter Mission

Following an initial trade-off on orbit design, a 320 km mean altitude low Mars orbit that is sun synchronous (SSO) was selected for the Mars Science Orbiter (MSO) mission. This orbit was selected because it does not have a strong synchronicity between orbital period and Mars rotation. This means that the ground track tightly covers the entire Mars surface after 7 days. Lower altitude orbits result in lifetime and planetary protection issues, whilst significantly higher orbits diminish the resolution of science data.

Trade-offs were also made on the Mars transfer scenario. Chemical, electric, and hybrid propulsion architectures were all considered as well as chemical kick stages and direct injection scenarios. Using a chemical kick stage would be an

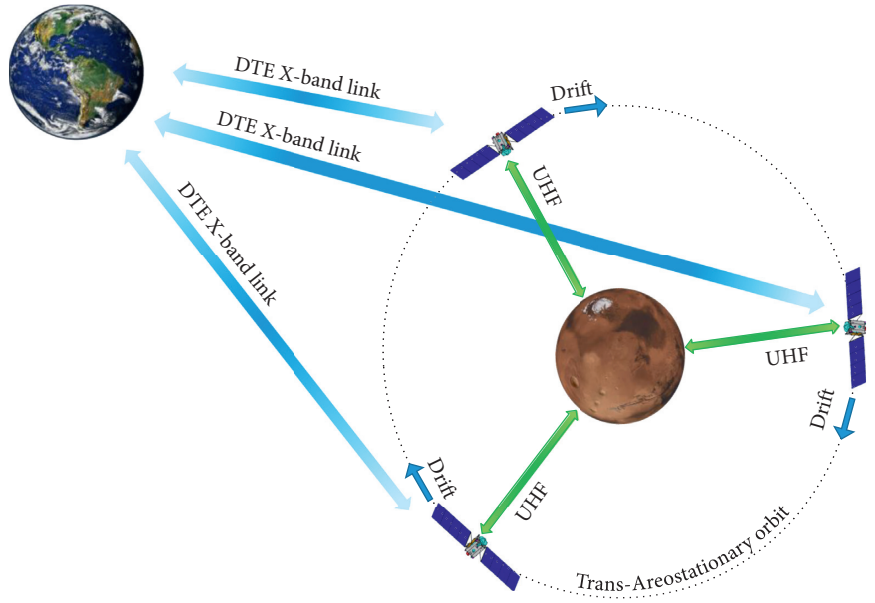

Figure 8: End-state architecture and communications concept for the Mars Communication Constellation mission.

Table 3: Science payload suite and associated objectives for the Mars Communications Constellation.

Instrument	Heritage	FOV (°)	Spatial Res. at TASO (m)	Science objective	Ref.
Wide-angle camera imaging suite (VIS)	VMC (Venus Express)	25 × 25	3840	Daily weather monitoring, dust storm, clouds	[18, 19]
Wide-angle camera imaging suite (NIR)	VMC (Venus Express)	25 × 25	3840	Atmospheric composition O_2, H_2O, CO, CO_2, N-species	[18, 19]
Wide-angle camera imaging suite (UV)	VMC (Venus Express)	25 × 25	3840	Ozone (250–270 nm), aurora effects	[18, 19]
Thermal IR radiometer	MARA (MASCOT)	5 × 5*	1.5*E*6*	Temperature of the atmosphere	[20]

Each satellite in the constellation contains an identical science payload suite. *An orbital version of MARA would need a modified optical design to obtain a 5° × 5° FOV instead of the original 18° × 18°. An upgrade to thermal IR imaging capability would be preferred if resources allow.

attractive option and one that would enable a rideshare launch to GTO. However, the costs and complexities involved in repurposing existing technologies to meet the mission requirements mean that it is no more costly and also programmatically simpler, to use a dedicated Ariane 62 launch to its full capability [21] with a large launch margin remaining for other opportunities.

The resulting reference launch and transfer scenario for this mission is thus to utilise a dedicated Ariane 62 launch to Earth escape, with the MSO satellite performing Mars Orbit Insertion (MOI) by way of an on-board chemical propulsion system. This scenario, along with estimated ΔV needs, is illustrated in Figure 9.

The end-state architecture of the constellation, including communications concept, is illustrated in Figure 10.

To select the science objectives, European and US priorities as stated in the MEPAG Science Objectives were considered [10]. The Mars Science Orbiter enables high-resolution imaging of the surface (e.g., fine-scale geology, mineralogy, resources, and topography) at two local times above the ground. High spatial resolution data (e.g., optical images, NIR infrared spectral data, thermal infrared, and terrain models) cover only a few percent of the surface. To better understand the planetary evolution of Mars and facilitate the selection of a scientifically rich and resource-rich landing site for human exploration missions, it is essential to fill the gaps in the spatial coverage and provide higher resolution data than is currently available.

Understanding the current distribution and form of water (e.g., liquid surface water, deep aquifers, water ice, and mineral-bound water) on the surface and in the subsurface of Mars is critical for interpreting the past aqueous history and the related paleoclimate. Orbital assets have identified various locations with hydrated mineral deposits such as phyllosilicates, sulfates, iron hydroxides/oxyhydroxides, carbonates, zeolites, and opal (e.g., [22, 23]). However, there is an uncertainty in the abundance, the composition variations at metre-scale resolution, and the mechanical properties of these deposits. This knowledge would be needed for in-situ resource utilisation (ISRU) purposes.

Additionally, the thermophysical properties of the regolith can provide information about the composition, grain

Table 4: Preliminary mass budget information for the Mars Communication Constellation mission.

		Mass (kg)
Attitude, orbit, guidance, navigation control		8.0
Chemical propulsion		6.9
Communication (UHF proximity link, DTE link: X-band, 50 W TWTA, 1 m HGA)		30.1
Electric propulsion (T6 engine)		70.4
Instruments		7.0
Power (2.8 kW @Mars for electric propulsion)		158.9
Structures		56.6
Thermal control		13.3
Data handling (0.5 Gb/day science data)		5.3
Harness		17.8
Dry mass		**374.3**
System margin	20%	74.9
Dry mass incl. system margin		**449.2**
CPROP propellant mass		4.7
CPROP propellant margin	2%	0.1
EPROP fuel mass (10.4 km/s ΔV)		153.8
EPROP fuel margin	2%	3.1
Wet mass (per satellite)		**610.9**
Constellation total dry mass incl. system margin		**1347.6**
Constellation total wet mass		**1832.7**
Launch adapter		360
Launch mass (wet mass + adapter)		**2192.7**

The bold values refer to summation values of the figures above them.

Figure 9: Launch and transfer scenario for the Mars Science Orbiter (MSO) mission.

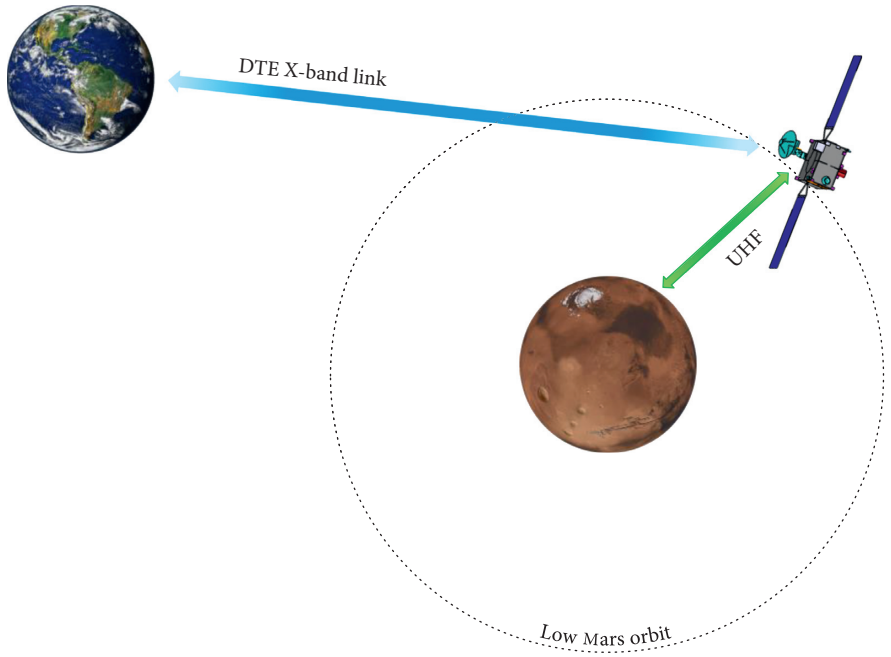

Figure 10: End-state architecture and communications concept for the Mars Science Orbiter mission.

sizes, rock distribution, surface roughness, porosity, and geological history of the surface ([24, 25]). The diurnal and seasonal changes in surface temperature are controlled by the thermal inertia. Thermal inertia depends primarily on the physical structure of the surface layer and is defined as a function of the thermal conductivity, heat capacity, and material density.

Moreover, change detection on the surface can allow monitoring of the dynamics of current surface processes including dune and ripple migration, landslides, dust deposition, and the recent impact flux.

Thus, the primary science goal was selected to map the thermophysical properties and the composition of the surface, focusing on hydrous minerals and to characterize surface hazards (e.g., rock abundance and high slopes) for future landed missions. The secondary science goal was to observe changes on the surface (e.g., new impacts, activities) inferring the current impact rate, dynamics of the surface processes, and the exchange between the surface and the atmosphere. As a summary, the following science objectives were considered:

(i) OBJ-01: characterize the thermophysical properties of the surface

(ii) OBJ-02: determine the spatial distribution of hydrated minerals on the surface

(iii) OBJ-03: constrain the timeline of geological history and habitability of Mars

(iv) OBJ-04: characterize surface hazards (e.g., rocks, slopes and incoherent material) to landing human scale systems

The science objectives from MEPAG Goal III (understand the origin and evolution of Mars as a geological system) (A1, A2, A3, A4) and Goal IV (prepare for human exploration) (A3/1, 2; C2/1) [10] can be addressed by the proposed MSO mission.

The primary payload of the Mars Science Orbiter mission is the science payload; however, the satellite also includes a data relay capability of similar sizing to the MCC satellites. To select the science payload, high TRL instruments from ESA's heritage planetary missions and European contributions to non-ESA missions were taken into account. Trade-offs were performed between (1) mass vs. performance and (2) maintaining heritage and optimising for the mission. The instruments and their associated science objectives are given in Table 5.

A preliminary design exercise shows that a wet mass of ~600 kg is feasible within the programmatic constraints. This allows for a total launch mass that is well within the capabilities of a dedicated Ariane 62 launch and also allows consideration of potential rideshare opportunities for small satellites or CubeSats. Mass reductions could be envisaged if the requirement to have a technology readiness level of 7/8 by PDR is relaxed or if a later launch opportunity is used. Conversely, mass increases could also be considered if it were to result in a significantly improved performance, so long as the programmatic constraints are still met. Key mass budget information is provided in Table 6. Note that a larger systems margin (30%) is used for chemical propulsion-based spacecraft than for an electric propulsion-based spacecraft (20%). This is the systems margin philosophy taken at this early phase of study and is due to mass growth seen in similar chemical systems over their development lifecycle.

5. Mars Hard Lander Mission

The study of the Mars Hard Lander (MHL) mission focussed mainly on mission analysis, entry, descent and landing (EDL), and cost. The reference mission architecture was chosen to comprise three hard landers, each with an entry mass of 70 kg and aiming to land 50 kg on the surface with an impact velocity of less than 20 m/s.

The entry mass of 70 kg draws large similarities with the *Beagle 2* lander on ESA's Mars Express mission (2003) which performed a semihard landing [31]. The study focussed on analysing if all the requirements could be met using the same aeroshell, parachutes, and EDL control as *Beagle 2*. The impact velocity requirement of less than 20 m/s was also derived from *Beagle 2* heritage. Using heritage equipment is in line with the main drivers for the mission: cost and schedule.

During the CDF study, the EDL trajectory and EDL equipment of the hard landers were analysed. Additionally, a high-level design of the carrier spacecraft was performed and a high-level cost estimation was made.

For the launch and transfer scenario, a dedicated Ariane 62 launch to $C_3 \approx 10\,km^2/s^2$ was used as a reference case, putting the landers on a ballistic coast towards Mars hyperbolic entry. This scenario is illustrated in Figure 11.

The landers are carried by a chemical propulsion carrier module with a top-level design allocation provided by a reduced capability version of the Mars Science Orbiter satellite (with a lower ΔV capability, for example, since there is no need for a Mars orbit insertion manoeuvre). Three hard landers were studied for redundancy reasons and to enable science that benefits from simultaneous measurements in different locations (e.g., weather monitoring, seismology).

Modelling of the EDL trajectory shows that, for a reference Mars arrival date of 2nd October 2029 and an entry velocity of 5.6 km/s, a flight path angle (FPA) of between -11° and -14° allows the impact velocity requirement to be met (≤20 m/sec at 0 km MOLA).

Using the peak heat flux and total heat load calculated, it could be analysed whether the thermal protection system (TPS) used on *Beagle 2* would be sufficient for the MHL. Due to the use of a shallower FPA (*Beagle 2* entered at -15.8° FPA), the MHL exceeds the heat load that *Beagle 2* was designed for. Therefore, additional TPS material would need to be added to the aeroshell. The mass of the additional material ranges from 5.17 to 0.67 kg for a FPA of -11° to -15°, respectively. The same pilot parachute and ringsail main parachute as *Beagle 2* are assumed and they have a diameter of 8 m and 10.4 m, respectively. Due to the high landing speed and high g-loads, a crushable attenuation structure is added to the lander. It was assumed to use the same material as ESA's Schiaparelli lander, which is an aluminium honeycomb sandwich structure. A trade between

Table 5: Science payload suite and associated objectives for the Mars Science Orbiter.

Instrument	Heritage	FOV (°)	Spatial res. at 320 km altitude (m)	Science objective	Ref.
Thermal IR radiometer/ Imaging spectrometer, imaging spectrometer, radiometer	MERTIS (BepiColombo)	4 × 4	<200 (imaging spectrometer), ≤2000 m (radiometer)	Surface composition, temperature, thermal inertia, rock abundance, atmospheric science	[26, 27]
Visible imaging system	CaSSIS (TGO)	1.35 × 0.85	3.2	High resolution colour imaging of the surface, change detection, stereo imaging, geological context	[28]
NIR spectrometer	MacrOmega (Mars Moon explorer) MicrOmega (Phobos-Grunt, Hayabusa-2, ExoMars 2022 rover),	*	*	Mineralogy	[29, 30]

The satellite also includes a data relay capability. *An orbital version of MicrOmega would need a different optical design as it would be focussed at infinity and use solar illumination; specification of the FOV and spatial resolution would depend on instrument-level design trade-offs.

Table 6: Preliminary mass budget information for the Mars Science Orbiter mission.

		Mass (kg)
Attitude, orbit, guidance, navigation control		8.0
Chemical propulsion		41.4
Communications (UHF proximity link, DTE link: X-band, 50 W TWTA, 1 m HGA)		34.3
Instruments		34.2
Power (310 W @Mars)		74.5
Structures		63.4
Thermal control		9.8
Data handling (730 Gb science data volume)		5.3
Harness		13.5
Dry mass SC		**284.4**
System margin	30%	85.3
Dry Mass SC incl. system margin		**369.7**
CPROP fuel mass (1370 m/s ΔV)		124.8
CPROP fuel margin	2%	2.5
CPROP oxidizer mass		97.7
CPROP oxidizer margin	2%	2.0
CPROP pressurant mass		1.0
CPROP pressurant margin	2%	0.0
Total wet mass SC		**597.7**
Launcher interface		64
Launched mass		**661.7**

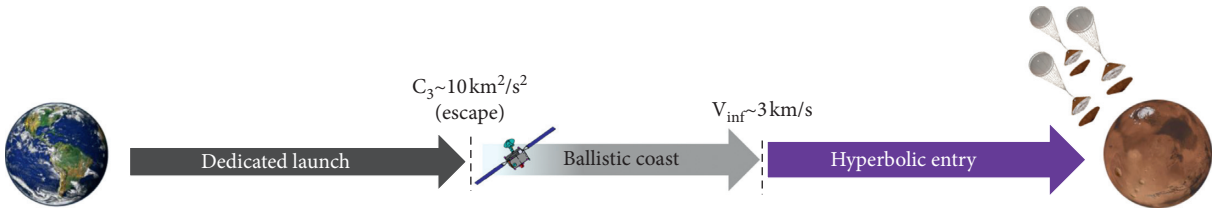

Figure 11: Launch and transfer scenario for the Mars hard lander mission.

the maximum allowable g-loads and the mass of the crushable structure led to a first estimation of allowable g-loads of 80g and 120g in the horizontal and vertical direction, respectively. Regarding EDL control, the same equipment as *Beagle 2* is considered for the Mars Hard Lander.

Using these assumptions, a preliminary mass budget is provided in Table 7. This budget is valid for an entry at flight path angles between −14° and −13°.

In order to achieve a spread in landing sites between the different hard landers, they need to be deployed from the carrier vehicle sequentially, whilst also leaving several

Table 7: Preliminary mass budget for the Mars Hard Lander mission.

Launch mass	**513 kg**
Wet mass carrier vehicle	303 kg
Entry probes (3)	210 kg
Entry probe	**70 kg**
EDL system	28.5 kg
Landed mass	41.5 kg
Science payload allocation	~9 kg

days between each lander deployment for navigation corrections and to adjust and confirm accuracy of the carrier trajectory. Therefore, the first lander probe has to be released up to 10 days before entering Mars orbit, meaning that it must survive without power from the carrier until it can deploy its solar panels on the surface of Mars. Thermal control by way of RHUs and the implementation of a low power (<10 mA) timer are enablers for the survival of multiday coasting landers. Additional fuel also has to be accommodated on the carrier in order to enable the trajectory adjustments.

6. Conclusions

Overall, the study identified a wide range of potential small Mars mission architectures including orbital and lander missions. From the resulting analysis, it appears that small, low-cost Mars missions are technically feasible for launch within the decade. Three main themes emerged in the conclusions of the study concerning the launch scenario, required technology developments, and the mission operations. In particular, a robust development schedule and selection of high-maturity technologies are critical to meeting the programmatic constraints of the mission.

A commercial rideshare to Earth orbit, while reducing launch costs, significantly drives the spacecraft design and mission operations. Any launch cost savings that are made when using a rideshare opportunity can be easily offset by additional spacecraft development and operations costs. Consequently, there are key technology developments in Europe that would help realise the benefits of commercial rideshare launches and reduce the overall cost of small Mars missions. These include high power, low mass solar arrays and low cost, low power and long lifetime EP thrusters. Until these developments are achieved, dedicated or dual launches will be more likely. Finally, the classical approach to mission operations becomes a substantial cost driver for small missions, especially for long duration transfers and time spent aerobraking. For a cost-driven mission, the approach taken to mission operations becomes a critical mission architecture design driver.

The work completed in this study of small Mars mission architecture will continue in 2021 with further study conducted by European industrial contractors.

6.1. The Concurrent Design Facility. The Concurrent Design Facility (CDF) is a state-of-the-art facility equipped with a network of computers, multimedia devices, and software tools, which allows a team of experts from several disciplines to apply the concurrent engineering method to the design of future space missions. It facilitates a fast and effective interaction of all disciplines involved, ensuring consistent and high-quality results in a much shorter time. It is primarily used to assess the technical and financial feasibility of future space missions and new spacecraft concepts (e.g., internal prephase A or Level-0 assessment studies). During this study, the CDF successfully transitioned to distributed remote operation mode, made necessary due to COVID-19 restrictions.

The Concurrent Design Facility was established at ESTEC in November 1998 within the framework of the General Studies Programme.

Data Availability

The Small Mars Mission Architecture Study (SMARTieS) CDF study report is available upon request from the authors.

Disclosure

An oral presentation of this manuscript was made at the Europlanet Science Congress (EPSC), 2020 [32].

Conflicts of Interest

The authors declare that there are no conflicts of interest regarding the publication of this paper.

Acknowledgments

This work was funded through the discovery element of ESA's Discovery, Preparation and Technology Development Programme.

References

[1] R.-M. Bonnet and J.-P. Swings, *The Aurora Programme. BR-214*, ESA Publications Division, Noordwijk, Netherlands, 2004.

[2] G. Cavallo, "European programmes the role of the European Space Agency in a small scientific mission programme," *Astra Astronaut*, vol. 39, no. 1–4, pp. 1–8, 1996.

[3] G. P. Whitcomb, "The ESA approach to low-cost planetary missions," *Acta Astronaut*, vol. 52, no. 2–6, pp. 79–86, 2003.

[4] G. Bagnasco, L. Giulicchi, P. Pablos et al., "The contribution of the science technology programme to low-cost planetary missions," *Acta Astronaut*, vol. 59, no. 8–11, pp. 882–898, 2006.

[5] R. Carli and P. Pablos, "System challenges in the development of low-cost planetary missions," *Acta Astronaut*, vol. 59, no. 8–11, pp. 1079–1085, 2006.

[6] European Space Agency, *Small Mars Mission Architecture Study (SMARTieS), CDF-205(A) CDF Study Report*, ESA, Noordwijk, Netherlands, 2020.

[7] J. J. Silva and P. Romero., "Optimal longitudes determination for the station keeping of areostationary satellites," *Planetary and Space Science*, vol. 87, pp. 14–18, 2013.

[8] L. Montabone and N. Heavens, *Observing Mars from Areostationary Orbit: Benefits and Applications, White Paper,*

submitted to the Planetary Science and Astrobiology Decadal Survey 2023–2032, https://mepag.jpl.nasa.gov/reports.cfm, 2020.

[9] E. Sefton-Nash, G. Thébault, O. Witasse, D. Koschny, B. Sánchez-Cano, and A. Cardesín-Moinelo, "Visibility analysis of Phobos to support a science and exploration platform," *Earth, Planets and Space*, in Review.

[10] MEPAG, "Mars scientific goals, objectives, investigations, and priorities: 2020," Edited by D. Banfield, Ed., White Paper Posted March, 2020 by the Mars Exploration Program Analysis Group (MEPAG), https://mepag.jpl.nasa.gov/reports.cfm, 2020.

[11] C. E. Newman, T. Bertrand, J. Battalio et al., "Toward more realistic simulation and prediction of dust storms on Mars: decadal survey on planetary science and astrobiology," White Paper, https://mepag.jpl.nasa.gov/reports/decadal2023-2032/DustStormsWhitePaper.pdf, 2020.

[12] N. G. Heavens, D. M. Kass, J. H. Shirley, S. Piqueux, and B. A. Cantor, "An observational overview of dusty deep convection in martian dust storms," *Journal of the Atmospheric Sciences*, vol. 76, no. 11, pp. 3299–3326, 2019.

[13] B. A. Cantor, "MOC observations of the 2001 Mars planet-encircling dust storm," *Icarus*, vol. 186, no. 1, pp. 60–96, 2007.

[14] M. S. Chaffin, J. Deighan, N. M. Schneider, and A. I. F. Stewart, "Elevated atmospheric escape of atomic hydrogen from Mars induced by high-altitude water," *Nature Geoscience*, vol. 10, no. 3, pp. 174–178, 2017.

[15] N. G. Heavens, A. Kleinböhl, M. S. Chaffin et al., "Hydrogen escape from Mars enhanced by deep convection in dust storms," *Nature Astronomy*, vol. 2, no. 2, pp. 126–132, 2018.

[16] Z. Girazian, Z. Luppen, D. D. Morgan et al., "Variations in the ionospheric peak altitude at Mars in response to dust storms: 13 years of observations from the Mars Express radar sounder," *JGR Planets*, vol. 125, no. 5, 2019.

[17] D. A. Glenar, R. E. Samuelson, J. C. Pearl et al., "Spectral imaging of martian water ice clouds and their diurnal behavior during the 1999 aphelion season (Ls = 130°)," *Icarus*, vol. 161, no. 2, pp. 297–318, 2003.

[18] W. J. Markiewicz, D. V. Titovad, N. Ignatiev et al., "Venus monitoring camera for Venus Express," *Planetary and Space Science*, vol. 55, no. 12, pp. 1701–1711, 2007.

[19] D. V. Titov, H. Svedhem, D. McCoy et al., "Venus Express: scientific goals, instrumentation, and scenario of the mission," *Cosmic Research*, vol. 44, pp. 334–348, 2006.

[20] M. Grott, J. Knollenberg, B. Borgs et al., "The MASCOT radiometer MARA for the Hayabusa 2 mission," *Space Science Reviews*, vol. 208, pp. 413–431, 2017.

[21] Ariane 6 User's Manual, Issue 1 Revision 0, March 2018, https://www.arianespace.com/wp-content/uploads/2018/04/Mua-6_Issue-1_Revision-0_March-2018.pdf.

[22] J.-P. Bibring, Y. Langevin, J. F. Mustard et al., "Global mineralogical and aqueous Mars history derived from OMEGA/Mars Express data," *Science*, vol. 312, no. 5772, pp. 400–404, 2006.

[23] J. Carter, F. Poulet, J.-P. Bibring et al., "Hydrous minerals on Mars as seen by the CRISM and OMEGA imaging spectrometers: updated global view," *JGR Planets*, vol. 118, pp. 831–858, 2013.

[24] R. L. Fergason, P. R. Christensen, and H. H. Kieffer, "High-resolution thermal inertia derived from the thermal emission imaging system (THEMIS): thermal model and applications," *Journal of Geophysical Research: Planets*, vol. 111, no. E12, 2006.

[25] M. T. Mellon, R. L. Fergason, and N. E. Putzig, "The thermal inertia of the surface of Mars," in *The Martian Surface*, J. Bell, Ed., Cambridge University Press, Cambridge, UK, 2008.

[26] H. Hiesinger and J. Helbert, "The Mercury radiometer and thermal infrared spectrometer (MERTIS) for the BepiColombo mission," *Planetary and Space Science*, vol. 58, no. 1-2, pp. 144–165, 2010.

[27] H. Hiesinger, J. Helbert, G. Alemanno et al., "Studying the composition and mineralogy of the hermean surface with the Mercury radiometer and thermal infrared spectrometer (MERTIS) for the BepiColombo mission: an update," *Space Science Reviews*, vol. 216, no. 110, 2020.

[28] N. Thomas, G. Cremonese, R. Ziethe et al., "The colour and stereo surface imaging system (CaSSIS) for the ExoMars Trace Gas Orbiter," *Space Science Reviews*, vol. 212, pp. 1897–1944, 2017.

[29] J.-P. Bibring, V. Hamm, Y. Langevin et al., "The MicrOmega investigation onboard Hayabusa2," *Space Science Reviews*, vol. 208, no. 1–4, pp. 401–412, 2017.

[30] C. Royer, J.-P. Bibring, V. Hamm et al., "The MacrOmega instrument on-board MMX, an ultra-compact NIR hyperspectral imager based on AOTF technology: preliminary tests on a breadboard," in *Proceedings of the 50th Lunar and Planetary Science Conference 2019 (LPI Contrib. No. 2132)*, The Woodlands, TX, USA, March 2019.

[31] J. Clemmet, M. Sims, N. Higgett et al., "Beagle 2 on Mars–the discovery assessed," *Journal of the British Interplanetary Society*, vol. 70, no. 8, pp. 261–304, 2017.

[32] C. E. Parfitt, A. McSweeney, A. J. Ball, L. De Backer, C. Orgel, and S. Vijendran, "Small Mars mission architectural study," *Europlanet Science Congress 2020*, vol. 14, 2020.